Characterization of a new dual-species atomic source for lithium and potassium

Adrian König, BSc

A Master thesis submitted to the
Faculty of Mathematics, Computer Science and Physics
of the University of Innsbruck

in partial fulfillment of the requirements for the degree of
Master of Science

Supervised by Univ.-Prof. Dr. Rudolf Grimm
Institute of Experimental Physics

November 2022

Abstract

In the FeLiKx experiment at the *Institute for Quantum Optics and Quantum Information* in Innsbruck, ultracold mixtures of lithium and potassium in the quantum-degenerate regime are investigated. This thesis contains the design and test of functionality of a new dual-species atomic beam source for that experiment. We investigate its emitted atomic beam regarding the transverse spectrum and the angular shape. The measurements are conducted by exciting the atoms with laser light and detecting the resulting flourescence. At the desired operating temperatures we conclude a total atomic flux of $\sim 5 \times 10^{12}\,\mathrm{s}^{-1}$ for potassium and $\sim 2 \times 10^{13}\,\mathrm{s}^{-1}$ for lithium. The beam shape of the atomic potassium beam for different temperatures is in agreement with the theoretical calculations. Our data for the center-line intensity allows us to calculate the peaking factor which is a measure for the efficiency of the source. Except for very low temperatures, it is in accordance with theory. From our data we can infer a lifetime of the source of at least five years before refilling is required.

Kurzfassung

Im FeLiKx Experiment am *Institut für Quantenoptik und Quanteninformation* in Innsbruck werden ultrakalte Quantengase aus Lithium und Kalium erforscht. Diese Masterarbeit dokumentiert das Design und den Funktionstest eines neuen Doppelspeziesatomstrahlofens für genau jenes Experiment. Wir untersuchen den emittierten Strahl bezüglich seines transversalen Spektrums und seines Winkelprofils. Die Messungen beruhen darauf, dass wir die emittierten Atome mit Laserlicht anregen und die dadurch entstehende Floureszenz detektieren. Bei den geplanten Betriebstemperaturen können wir auf einen Atomfluss von $\sim 5 \times 10^{12}\,\mathrm{s}^{-1}$ für Kalium und $\sim 2 \times 10^{13}\,\mathrm{s}^{-1}$ für Lithium schließen. Das Profil des Strahls aus Kaliumatomen bei verschiedenen Temperaturen deckt sich mit unseren theoretischen Berechnungen. Unsere Messdaten für die Intensität auf der Mittelachse erlauben es uns den Kollimationsfaktor zu berechnen, welcher ein Maß für die Effizienz unserer Atomquelle darstellt und abgesehen von sehr niedrigen Temperaturen gut mit unserer Theorie übereinstimmt. Aus unseren Daten können wir eine Betriebszeit des Ofens von mindestens fünf Jahren ableiten, bevor ein Nachfüllen von Atomen notwendig wird.

Contents

1 Introduction

Since physicists suceeded in trapping neutral atoms using laser light in 1986 and achieving the first magneto-optical trap (MOT) in 1987, the methods used have evolved enormously [Chu86; Raa87]. In the following years, additional techniques for cooling the trapped atoms were developed with the help of which the first Bose-Einstein condensate of rubidium atoms could be created in 1995 [And95]. This sensation launched the era of ultracold, quantum degenerate gases. A total of fifteen atomic species have been successfully Bose-Einstein condensed since, with erbium, thulium and europium being the three most recent ones, that joined in 2012, 2020 and 2022, respectively [Fri12; Dav20; Miy22].

As quantum degeneracy for fermions cannot be achieved quite as easily as for bosons due to the Pauli exclusion principle, experiments were started with two species involved. The idea here is to sympathetically cool the atoms by use of the other species. One of the experiments exploiting this trick is the FeLiKx experiment here in Innsbruck, which works with a mixture of lithium and potassium atoms [Wil09]. But also quantum degenerate mixtures of e.g. Na-Li [Heo12], Cs-Yb [Kem16], K-Dy [Rav18], Er-Dy [Tra18], or Li-Cr [Ner20] have been realized and are under investigation. Additionally, mixtures do not only facilitate the quantum degeneracy of fermions but also open up a whole new field of physics to be explored. They allow to study fermions together with bosons in one sample [Mod02; Fri21] and interspecies Feshbach resonances enable the creation of quasi particles like the Polaron [Spi10; Koh12]. Moreover, the effect of mass imbalance can be investigated. Many of those experiments have proven to be extremely useful as quantum simulators.

Even though each of the experiments mentioned works with different species and might pursue different scientific goals, their basic setup is similar. At the beginning there has to be a device providing the gaseous atoms of the desired species. For elements like Rb or Cs this is quite easy as their melting temperatures are just above room temperature. On the other extreme there are lanthanides like Er or Dy having melting temperatures way higher than 1000 °C. Therefore, it has become an inevitable challenge in the field to build an appropriate oven evaporating the species [Sta05; Sch12; Sen15; Bow16]. The physics behind the process of an atomic vapour escaping a reservoir though has nothing to do with state of the art quantum technology. Many of the equations used have been known since the beginning of the last century, which makes it rather an engineering task. Nevertheless, as ultimately the loading of the atomic trap and such the quality of the whole experiment is limited by the oven, its functionality is crucial for any ultracold atom lab. In the FeLiKx experiment the oven providing the beam of lithium and potassium atoms does not work as good as theoretically expected. Its emitted atomic flux of potassium arriving at the MOT is about 10^4 times lower

than calculations predict which is why a new device has become necessary.

This thesis describes the design and test of functionality of a new kind of dual species atomic source for lithium and potassium. Therefore, chapter 2 summarizes the theoretical foundation of effusive sources. The process of beam formation is explained for different types of operation of the source and corresponding design criteria are deducted. In chapter 3 the problems with our current oven are explained. Tyring to avoid them to reappear leads to the most important considerations for the new design. The setup built to test the oven is shown in chapter 4. As the measurements are based on atomic flourescence, our photomultiplier tube is the core of the devices used. Chapter 5 shows our measurements of the transverse spectra we took right behind the oven nozzle. From these spectra we can deduct the absolute number of atoms leaving the oven depending on its temperature. In order to gather knowledge about their angular distribution, we measure the atomic beam shape at a larger distance to the oven nozzle. These measurements are shown in chapter 6 together with an absolute determination of the intensity on the beam axis. This allows us to conclude on the efficiency of the source, which is important for the loading rate of the MOT. A new oven providing a collimated atomic beam with high flux is going to decrease the MOT loading time in every experimental cycle. Consequently, future measurements in the FeLiKx lab will speed up significantly.

2 Effusive Sources

In this chapter the theoretical foundation of effusive sources is discussed. Essential parameters to describe the emitted atomic beam are introduced and their dependence on different ways of operation is explained. For our explanations we mainly stick to the formalism presented in Ref. [Bei75]. From these considerations one can deduct important aspects for the design of such a source regarding its beam formation and efficiency. Additionally, the velocity distribution of the emitted atoms is briefly touched upon.

2.1 Cosine emitter

The easiest kind of an effusive source consists of a reservoir with the atoms as a gas or vapour in it and an orifice through which they can escape as shown in Fig. 2.1. Mathematically, the emitted atoms are described by their intensity distribution $I(\vartheta)$ which is the number of atoms passing the orifice per second into a solid angle $\mathrm{d}^2\Omega$ under an angle ϑ relative to the beam axis. The integral of the intensity distribution over the half space equals the total number of atoms that leave the reservoir per second

$$\dot{N} = \int_{2\pi} I(\vartheta)\,\mathrm{d}^2\Omega \tag{2.1}$$

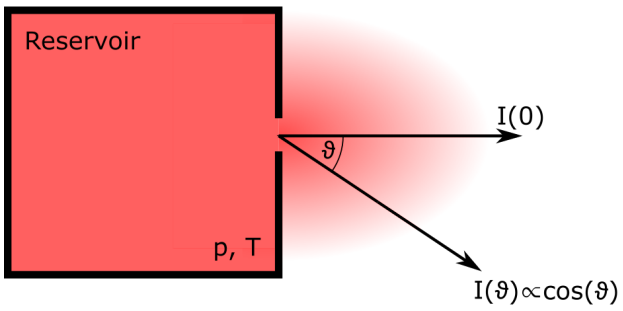

Figure 2.1: Sketch of a reservoir filled with an atomic vapour at temperature T and pressure p. The orifice is a thin-walled hole. In this case, the intensity distribution of the emitted atoms $I(\vartheta)$ scales with the cosine of the angle relative to the beam axis.

and is called the total atomic flux [Bei75]. It depends linearly on the density of the vapour in the reservoir

$$n = \frac{p}{k_\mathrm{B} T}, \tag{2.2}$$

the mean velocity of the atoms $\bar{v} = \sqrt{8 k_\mathrm{B} T / \pi m}$ deduced from the Maxwell-Boltzmann distribution and the area of the orifice A

$$\dot{N} = \frac{1}{4} n \bar{v} A. \tag{2.3}$$

Here k_B is the Boltzmann constant, T the temperature of the gas and p its pressure. The mass of the atomic species is m.

If the orifice is realized by a thin-walled hole like in Fig. 2.1 the distribution of the beam intensity is given by

$$I(\vartheta) = I(\vartheta = 0) \times \cos(\vartheta) = \frac{\dot{N}}{\pi} \cos(\vartheta), \tag{2.4}$$

which is where the name 'cosine emitter' is derived from. The center-line intensity $I(\vartheta = 0)$ is the intensity on axis with the beam. We explicitely neglect the dependence on the azimuth angle φ and always assume the emitted beam to be rotationally symmetric (due to rotational symmetry of the aperture). According to Eq. (2.4) the intensity scales with $\cos(\vartheta)$ which means that for $\vartheta = 60°$ the beam intensity is still half of the one on axis $I(0)$. In other words a lot of atoms emerge at large angles. In order to have a quantitative measure of how collimated the emitted beam is, one can define the efficiency of the source

$$\eta = \frac{\dot{N}(\vartheta \leq \vartheta_\mathrm{max})}{\dot{N}} = \frac{2\pi}{\dot{N}} \int_0^{\vartheta_\mathrm{max}} I(\vartheta) \sin(\vartheta) \, \mathrm{d}\vartheta, \tag{2.5}$$

which is the ratio of the flux up to a certain angle ϑ_max to the total flux. The magnitude of this maximum angle depends on what the atomic beam is intended to be used for, but usually experiments benefit from a highly collimated beam. In the FeLiKx experiment the atoms pass a Zeeman slower tube with radius $r = 7\,\mathrm{mm}$ and get captured by a MOT with an effective distance $D = 1.7\,\mathrm{m}$ to the oven afterwards. Hence, only atoms that emerge at angles $\vartheta \leq \vartheta_\mathrm{max} = 0.24°$ are useful for the experiment and contribute to the MOT loading. Plugging this maximum angle and the intensity distribution of a cosine emitter from Eq. (2.4) into Eq. (2.5), we end up with an efficiency of 1.7×10^{-5}. Consequently, using a cosine emitter at FeLiKx would result in not even two atoms out of one hundred thousand reaching the MOT.

To decrease the angle of half intensity, thus improving efficiency, an intuitive modification is to replace the thin-walled orifice by a tube with length L and radius a as shown in Fig. 2.2. For this altered design three modes of operation exist depending on the pressure within the reservoir: the transparent regime, the opaque regime and the viscous regime. The parameter to distinguish them is the mean free path of the atoms

$$\lambda_\mathrm{mf} = \frac{1}{\sqrt{2} n \sigma_\mathrm{col}}. \tag{2.6}$$

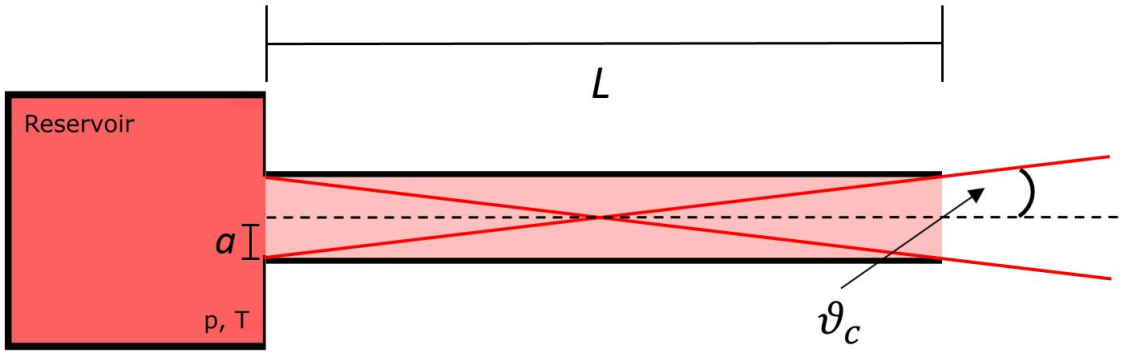

Figure 2.2: In order to increase beam collimation, the thin-walled aperture is replaced by a tube with radius a and length L. Atoms emerging at angles less than ϑ_c are not subject to collisions with the wall of the tube.

It equals the average distance an atom can travel before colliding with another atom of its species and depends on their collisional cross-section σ_{col} and on the density of the atomic vapour according to Eq. (2.2). For a mean free path larger than the geometric dimensions of the tube the oven is operated in the transparent regime:

$$\lambda_{\mathrm{mf}} \gg L, a \quad \text{(transparent regime)}. \tag{2.7}$$

In this regime the number and hence the density of the atoms passing through the tube is so low that atom-atom collisions are negligible and predominantly collisions with the wall of the tube happen.
In contrast, the atoms primarily collide with each other for high pressures within the reservoir and their dynamics follow the laws of continuum flow. Here the mean free path is small compared to the geometric dimensions of the tube and this case is called the viscous regime:

$$\lambda_{\mathrm{mf}} \ll L, a \quad \text{(viscous regime)}. \tag{2.8}$$

For the mean free path being smaller than the length of the tube but still larger than its radius the source is in the opaque regime. This is the intermediate case where interatomic collisions come into play but the intensity distribution of the emitted atoms is still governed by wall collisions:

$$a < \lambda_{\mathrm{mf}} < L \quad \text{(opaque regime)}. \tag{2.9}$$

In the following two sections the transparent and opaque regime are discussed. The case of viscous flow is omitted since we do not intend to operate our oven in this regime.

2.2 Transparent regime

For low densities within the reservoir leading to mean free paths larger than the dimensions of the tube ($\lambda_{\mathrm{mf}} \gg L, a$) the source is operated in the transparent regime. The emerging atoms only collide with the wall of the tube as collisions amongst them are negligible. For atoms that emerge on axis ($\vartheta = 0$) the additional tube does not change anything compared to the thin-walled aperture, which is why the center-line intensity is the same as in the cosine emitter case

$$I(0)_{\mathrm{tr}} = I(0)_{\cos} = \frac{1}{4\pi} n\bar{v}(\pi a^2) \tag{2.10}$$

with the area being equal to the cross section of the tube. All other atoms can be intuitively divided into two groups. As the demarcation between them serves the critical angle

$$\vartheta_{\mathrm{c}} = \arctan\left(\frac{2a}{L}\right) \tag{2.11}$$

given by the tube dimensions as can be inferred from Fig. 2.2. In this thesis the atoms with $\vartheta < \vartheta_{\mathrm{c}}$ are called type I atoms and they can pass the tube without colliding with its wall. By contrast, the path of flight of the other type of atoms (type II) with $\vartheta > \vartheta_{\mathrm{c}}$ gets interrupted by the tube and they collide with its wall at least once before leaving it. For the collisions with the wall we always assume diffuse reflections such that the probability of getting reflected towards the end of the tube is the same as for getting reflected back towards the reservoir [Cla30a].

Accordingly, the total flux $\dot{N}$ is diminished by the probability of passing through the tube called Clausing factor W:

$$\dot{N}_{\mathrm{tr}} = \dot{N}_{\cos} \times W. \tag{2.12}$$

This factor only depends on the geometry of the tube and in case of a cylindrical shape it is determined by [Cla32]

$$W = \frac{{}^{8a}/_{3L}}{1 + {}^{8a}/_{3L}}. \tag{2.13}$$

One can already see that for a short tube in the sense of a large diameter compared to its length ($a \gg L$) Eq. (2.13) converges towards unity like in the cosine emitter case. In the other extreme of a long and narrow tube ($a \ll L$) it can be approximated with the simplified expression $W \approx 8a/3L$. The derivation of Eq. (2.13) is is done by geometric considerations and can be found in [Cla32].

Nevertheless, one can get a qualitative feeling by modelling the passage of an atom through the tube by a so-called random walk. In this scenario the entrance to the tube is at position $z = 0$ and the end of the tube at $z = L$. The atom starts at an initial position $z \in [0, L]$ and in each step it can either go a discrete step to the left or right each with probability $p^- = p^+ = 0.5$, which illustrates the diffuse reflections on the wall of the tube. Let $P_L(z)$ be the probability that an atom at position z reaches the end of the tube at position $z = L$ without ever going back to $z = 0$ which resembles the Clausing factor W of passing through

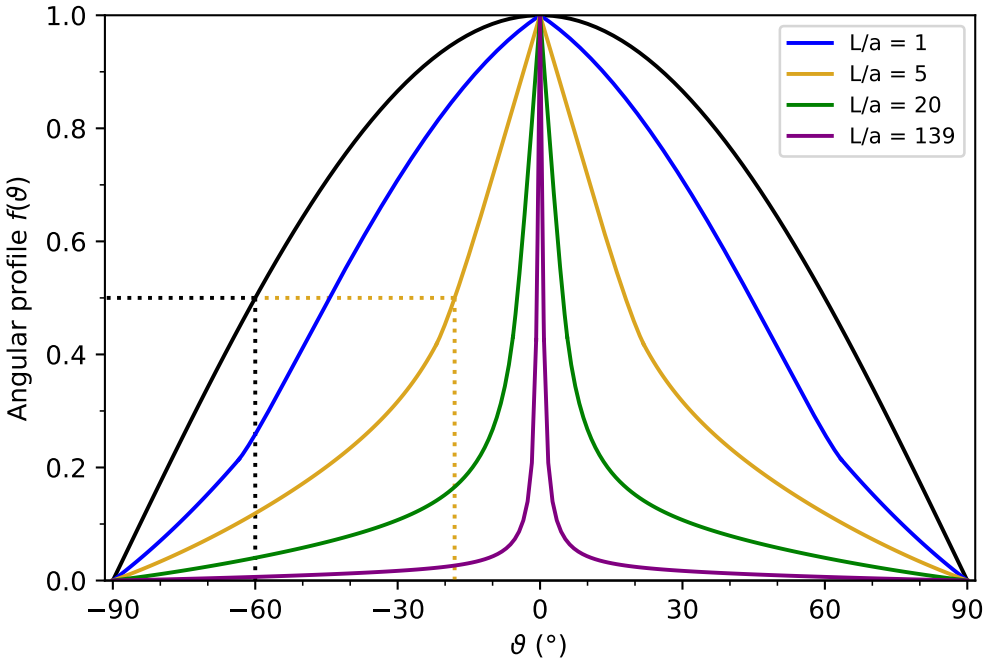

Figure 2.3: Angular profile $f(\vartheta) = I(\vartheta)/I(0)$ for different aspect ratios of the tube. The black curve represents a cosine emitter with $f(\vartheta) = \cos\vartheta$. The ratio $L/a = 139$ is the one for the lithium tubes of the new oven. The dashed lines stress the decrease of the angle of half-intensity for increasing aspect ratio.

the tube. In statistics this scenario is known as *gambler's ruin* and its simple solution is $P_L(z) = z/L$, a probability increasing linearly with the initial position of the atoms towards the end. For the assumption of a long and narrow tube thus the proportionality of $W \propto L^{-1}$ is recovered.

As the center-line intensity does not change due to the tube but the total flux does, also the intensity distribution $I(\vartheta)$ must be different compared to the case without tube. A convenient way of writing the intensity distribution is

$$I(\vartheta) = \frac{\dot{N}}{\pi}\kappa f(\vartheta) = I(0)f(\vartheta) \tag{2.14}$$

which introduces two new quantities [Bei75]. First, the peaking factor

$$\kappa = \pi\frac{I(0)}{\dot{N}} \tag{2.15}$$

that represents the ratio of center-line intensity to total flux and is a useful measure for how efficient a certain source is. The factor of π is due to normalization, such that $\kappa = 1$ for the case of a cosine emitter. In the case of a tube one can combine Eq. (2.10) and Eq. (2.12) to infer that $\kappa = W^{-1}$.

Second, the angular profile which is defined as the intensity distribution normalized to its magnitude on the center-line:

$$f(\vartheta) = \frac{I(\vartheta)}{I(0)}. \tag{2.16}$$

Correspondingly, the angular profile for the cosine emitter is simply $f(\vartheta) = \cos(\vartheta)$ and $f(0) = 1$ in any case. For a tube operated in the transparent regime the expressions are not as straightforward anymore. Atoms emerging at angles $\vartheta > \vartheta_c$ are distributed according to

$$\kappa f(\vartheta) = \frac{\cos^2(\vartheta)}{\pi \sin(\vartheta)} \frac{8a/3L}{W} (1 - W) + \frac{\cos(\vartheta)}{2} \tag{2.17}$$

and for angles $\vartheta < \vartheta_c$

$$\kappa f(\vartheta) = \frac{2\cos(\vartheta)}{\pi W} \left[\left(1 - \frac{W}{2} \right) R(p) + \frac{2}{3}(1 - W) \frac{1 - (1 - p^2)^{3/2}}{p} \right] + \frac{\cos(\vartheta)}{2} \tag{2.18}$$

with $R(p) = \arccos(p) - p\sqrt{1 - p^2}$ and $p = \tan(\vartheta)L/(2a)$ [Cla30b; Ola70]. Here it is remarkable that the angular distribution only depends on geometrical quantities, namely length and radius of the tube. In Fig. 2.3 the angular profile is plotted for several aspect ratios of the tube. While in the cosine emitter case (black line) the HWHM is still at 60°, it already shrunk to roughly 18° for $L/a = 5$ (yellow line) as indicated by the dotted lines.

Likewise, one can compare the efficiency of a cosine emitter with tubes of different aspect ratio. To do so, one numerically integrates Eqs. (2.17) and (2.18) according to Eq. (2.5). In Fig. 2.4 the resulting efficiency depending on the tube aspect ratio is plotted for $\vartheta_{max} = 0.24°$, which is the maximum angle at the FeLiKx experiment due to radius and distance of the MOT chamber. As this maximum angle is the limiting quantity in this calculation, it is instructive to scale the aspect ratio in multiples of D/r which is done in the top axis of the plot. For small L/a the efficiency increases linearly before the slope starts to decrease in the regime where $L/a \approx D/r$. For large aspect ratios the slope further decreases until the efficiency converges towards a fixed value less than unity. In order to understand this behaviour we take a look at the limiting cases. In the limit of a short tube or in mathematical terms $L/a \ll D/r$ the half-width of the angular distribution is large and the atoms that eventually reach the target are mainly of type I, the ones that do not collide with the wall of the tube. So the efficiency is in good approximation given by the center-line intensity which according to Eq. (2.15) itself is linear with the peaking factor κ. As for cylindrical tubes $\kappa = W^{-1}$, the peaking factor is approximately linear in L/a and enhances the efficiency compared to the cosine emitter case

$$\eta \approx \kappa \times \eta_{\cos} \tag{2.19}$$

which is illustrated by the blue dashed line.

In the other limit of long tubes ($L/a \gg D/r$) the atoms reaching the target are mainly of type II, as the probability of passing the tube without collisions decreases and the angular

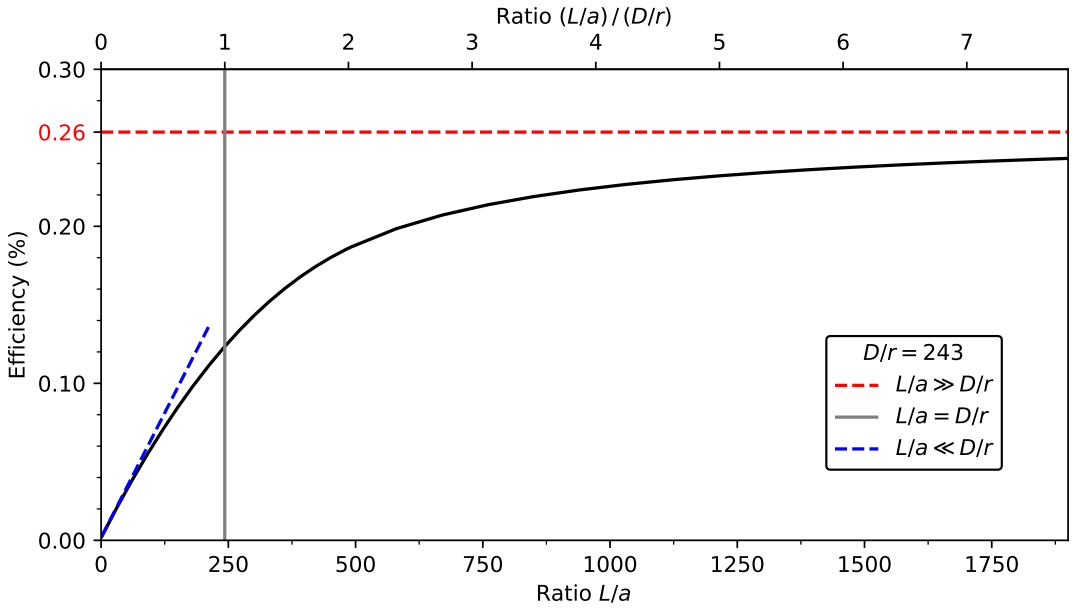

Figure 2.4: Efficiency of an atomic beam source at the FeLiKx experiment depending on the aspect ratio of the tube attached to it. The ratio D/r is the distance to the target the atoms are supposed to hit divided by its radius.

distribution gets independent of the aspect ratio itself. So we neglect the term for small angles in the integration, exploit the trigonometric small-angle approximation and end up at

$$\eta \to \frac{2}{\pi}\frac{r}{D} + \frac{1}{2}\left(\frac{r}{D}\right)^2 = 0.263\,\%. \tag{2.20}$$

Due to the long distance of 1.7 m to the MOT chamber and the small radius of 7 mm of the Zeeman slower tube, the efficiency in the FeLiKx experiment is eventually limited to roughly 0.26 %, which is represented by the red dashed line in Fig. 2.4. But nevertheless, choosing a tube aspect ratio of $L/a = D/r$ results in an efficiency enhancement of roughly a factor 70 compared to the cosine emitter case. Not even two orders of magnitude might not sound too much but it is. First, buying seventy times more atoms does make a difference especially for expensive isotopes. Second, the reduced loading time for the MOT allows to take more data in the same time. And third, reloading the oven seventy times less often reduces efforts of maintenance drastically.

2.3 Opaque regime

As the total flux scales linear with the density in the reservoir it suggests itself to further increase the pressure in order to obtain higher center-line intensities. But this fails as the increased density within the tube affects the mean free path of the atoms. So far, collisions between atoms have been neglected due to the low density within the tube. Then, the intensity distribution as well as the efficiency of the source have only been determined by

geometric quantities. The efficiency was independent of the flux emerging from the oven and the flux itself scaled linear with the density in the reservoir. But as soon as the mean free path is smaller than the tube length ($L \geq \lambda_{\mathrm{mf}} > a$) due to an increased density within the reservoir according to Eq. (2.6), one enters the opaque regime and interparticle collisions come into play. They intuitively mainly affect type I atoms which pass the tube without wall collisions, while type II atoms are subject to collisions anyway. Consequently, type I atoms that now start to suffer from collisions with other atoms cannot contribute to the center-line intensity anymore. Compared with the transparent case the center-line flux gets diminished where for larger angles the atomic distribution (in a good approximation) stays unaffacted.

For a mathematical model, Hanes introduced the relative driving pressure $P = p/p_0$, where p is the pressure in the reservoir and p_0 is a reference pressure that is defined such that the corresponding mean free path equals the length of the tube: $\lambda_{\mathrm{mf}}[n(p_0)] = L$ [Han60]. So for $P > 1$ the source is operated in the opaque regime. Via Eq. (2.2) this reference pressure can be converted into a reference density n_0 that can be written as

$$n_0 = \frac{1}{\sqrt{2} L \sigma_{\mathrm{col}}} \tag{2.21}$$

using Eq. (2.6). Say that the exit of the tube is at $z = 0$ and its entry at $z = L$. Now the idea is that the density decreases throughout the tube and at a certain position $z = L'$ it has a magnitude such that the local mean free path equals the remaining length of the tube L':

$$\lambda_{\mathrm{mf}}[n(L')] \stackrel{!}{=} L'. \tag{2.22}$$

Next, one can imagine a new beam being emitted from this surface through a tube with an effective length L' and radius a but operated in the transparent regime. Subsequently, the center-line intensity decreases because the aspect ratio decreased due to the shorter tube. This is why in the opaque regime we expect a diminished $I(0)$ compared to the same tube operated in the transparent regime.

To quantify this attenuation, Giordmaine et al. suggested and Kurepa et al. validated that one can model the atomic density linearly over the length of the tube as long as $\lambda_{\mathrm{mf}} > 2a$ [Gio60; Kur81]:

$$n(z) = n \times \frac{z}{L} \quad \text{with } z \in [0, L]. \tag{2.23}$$

Certainly, this linear model suffers from the problem of yielding a density of zero at the tube exit which cannot be true obviously [Ola70]. For our calculations nevertheless this approximation is good enough. Therefore, using this linear model, the condition from Eq. (2.22) and the reference density n_0 from Eq. (2.21) we can calculate

$$n(L') = \frac{n}{L} \frac{1}{\sqrt{2}\sigma_{\mathrm{col}} n(L')} \Longrightarrow n(L') = \sqrt{n \times n_0}. \tag{2.24}$$

Introducing the reduced density $n^* = n/n_0$ and plugging the above result for $n(L')$ into Eq. (2.10)

$$I(0)_{\mathrm{op}} = I(0)_{\mathrm{tr}} \times \frac{1}{\sqrt{n^*}} \tag{2.25}$$

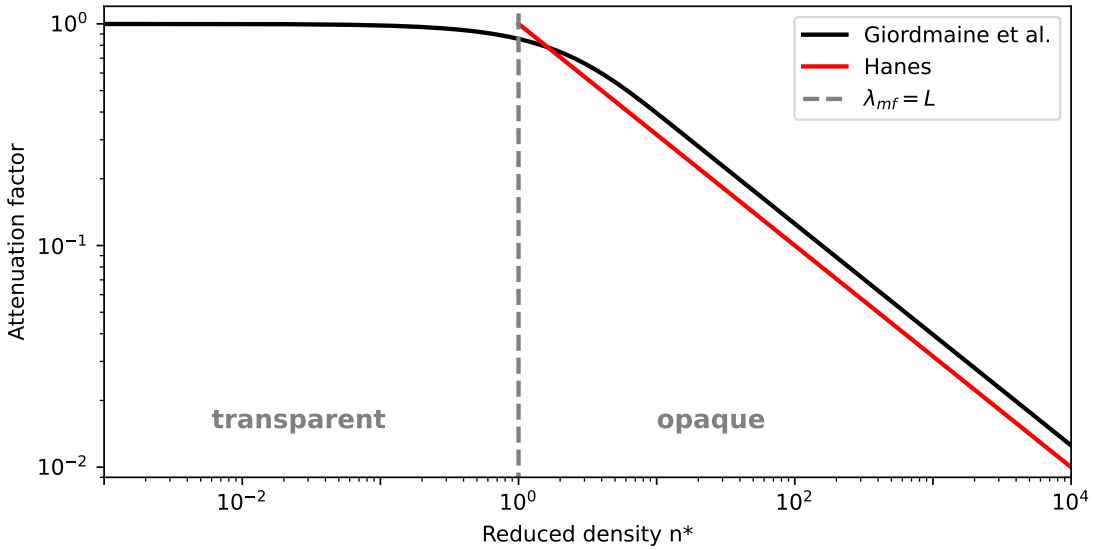

Figure 2.5: Attenuation factor of the center-line intensity depending on the reduced density n^* according to the simple model of a reduced tube length L' and to Giordmaine et al., respectively. The dashed gray line marks the border between transparent and opaque regime at $n^* = 1$.

we can see that the center-line intensity now gets scaled down by a factor of $1/\sqrt{n^*}$ compared to a tube with length L' operated in the transparent regime. The reduced density can also be written as

$$n^* = \frac{n}{n_0} = \frac{L}{\lambda_{\mathrm{mf}}} \tag{2.26}$$

and is thus (as it equals the ratio of length to mean free path) an intuitive quantity for the opaqueness of a tube. Increasing the pressure within the reservoir (above the border of transparent to opaque regime) hence leads to a decrease in center-line intensity and by implication also in peaking factor and efficiency as the higher pressure results in a higher density leading to a higher reduced density.

A more accurate solution for the attenuation factor was deduced by Giordmaine et al.

$$A(n^*) = \frac{\sqrt{\pi}}{2}\sqrt{\frac{2}{n^*}} \times \mathrm{erf}\left(\sqrt{\frac{n^*}{2}}\right) \tag{2.27}$$

such that the center-line intensity can be written as $I(0)_{\mathrm{op}} = A(n^*) \times I(0)_{\mathrm{tr}}$ [Gio60]. In Fig. 2.5 the model of Giordmaine et al. is plotted together with the simpler model of Hanes who simplified the tube in opaque operation by a shorter tube in transparent operation. Already for reduced densities larger than $n^* \geq 6$ the two models only differ by a constant factor of $\sqrt{\pi/2} \approx 1.25$.

These calculations stop to be valid at the point where the density within the reservoir has increased so much that the mean free path is smaller than the radius of the tube. At this

point the continuum or viscous flow regime starts which is not treated in this thesis as it does not play a role for effusive sources used in ultracold atomic labs.

In conclusion, as soon as the opaque regime is entered due to an increasing atomic density, center-line intensity as well as peaking factor and efficiency start to drop and are as well as the intensity distribution a function of the driving pressure. In contrast, the flux still remains a linear function of the density. For this reason operating an atomic source on the border from transparent to opaque regime is supposed to yield a high atomic flux with maximum efficiency.

2.4 Velocity distribution

After the atoms emerge from the oven they travel with a velocity that is orders of magnitude too high for them being trapped by the MOT. For this reason they pass a Zeeman slower as a first cooling stage whose design primarily depends on the velocity of the atoms. In the reservoir the velocities of the atomic vapour follow a standard Maxwell-Boltzmann distribution peaked at $\alpha = (2k_\mathrm{B}T/m)^{1/2}$ with a mean velocity of

$$\bar{v} = \frac{2}{\sqrt{\pi}}\alpha. \tag{2.28}$$

This is not true anymore as soon as we look into the beam emerging from the oven. Intuitively, fast atoms leave the reservoir earlier than slow ones. That is why per unit time more fast atoms escape and the velocities in the beam must be higher accordingly. They are distributed according to a modified Maxwell-Boltzmann distribution

$$F(v) = \frac{2}{\alpha^4} v^3 \mathrm{e}^{-v^2/\alpha^2} \tag{2.29}$$

now scaling with the third power of the velocity and peaked at $\alpha_\mathrm{beam} = 1.22\,\alpha$ [Ram85]. Consequently, also the mean atomic velocity in the beam is enhanced compared to a volume of gas by

$$\bar{v}_\mathrm{beam} = 0.75\sqrt{\pi}\,\alpha \approx 1.33\,\alpha. \tag{2.30}$$

The Zeeman slower has a so-called capture velocity v_c which is the highest velocity it is able to slow down and which depends on its length, the magnetic field applied, the effective magnetic moment of the two states addressed and the respective wave vector. As a result, its efficiency simply equals the integral over the velocity distribution of the incoming atoms up to the capture velocity

$$\eta_\mathrm{zee} = \int_0^{v_\mathrm{c}} F(v)\,\mathrm{d}v = 1 - \left(1 + \frac{v_\mathrm{c}^2}{\alpha^2}\right) \exp\left(-v_\mathrm{c}^2/\alpha^2\right). \tag{2.31}$$

The capture velocities of the Zeeman slower incorporated in the FeLiKx experiment are $927\,\mathrm{m\,s^{-1}}$ for ^{6}Li, resulting in an efficiency of $\eta_\mathrm{zee}^\mathrm{Li} = 11.6\,\%$ at $T_\mathrm{Li} = 350\,^\circ\mathrm{C}$ and $334\,\mathrm{m\,s^{-1}}$ for ^{41}K, yielding $\eta_\mathrm{zee}^\mathrm{K} = 16.3\,\%$ at $T_\mathrm{K} = 90\,^\circ\mathrm{C}$.

3 The oven at FeLiKx

This chapter outlines the issues we have with our current oven and concludes on requirements the new one has to fulfill besides from preventing the known problems to reappear. Based on these demands some considerations that contributed to the new design are explained and their actual realization is presented.

3.1 Drawbacks of the current oven

The current oven providing the atomic beams of lithium and potassium for the FeLiKx experiment has been running since its implementation in 2007. The flux of the atomic potassium beam to the MOT is roughly a factor of 10^4 lower than theoretically expected. This poor performance might be attributed to a known problem of evaporating alkalis that was already found in 1931: the effect of wicking [Lew31]. But also in more recent experiments e.g. from 2016 this effect still causes problems for the scientists [Bow16]. In our case we assume that the liquid lithium gets pulled into the microtubes due to capillary action and thus clogs the tubes. This assumption is supported by the fact that through a viewport after the oven one can see distinct stains of solid lithium sticking to the inner wall of the vacuum chamber. Unfortunately, there is no possibility to monitor the oven output from the outside which makes it hard for us to get a more detailed idea of what is really going on inside.

A further technical disadvantage is that the heating is done from outside of the vacuum. On the one hand, this is unfavorable as it is quite inefficient and no optics can be placed near the oven due to convection currents. On the other hand, this results in a very inaccurate determination and control of the actual temperatures within the oven and its tubes. Moreover, this makes it harder, and in our case impossible, to obtain the desired temperature gradient between the regions where the different elements melt.

A problem the potassium reservoir suffers from is its reloading. The atoms are stored within a glass ampulla that is put into the reservoir. In order to release them the reservoir has to be squeezed such that the ampulla breaks. This method combined with frequent reloading and temperature cycling stresses the vacuum seals and has already led to leaks. As in the end all of the points mentioned above contribute to the bad functionality, a new oven with a new design had to be developed. This new design is supposed to circumvent the existing problems, prevent them from reappearing and assure a smooth long-term operation.

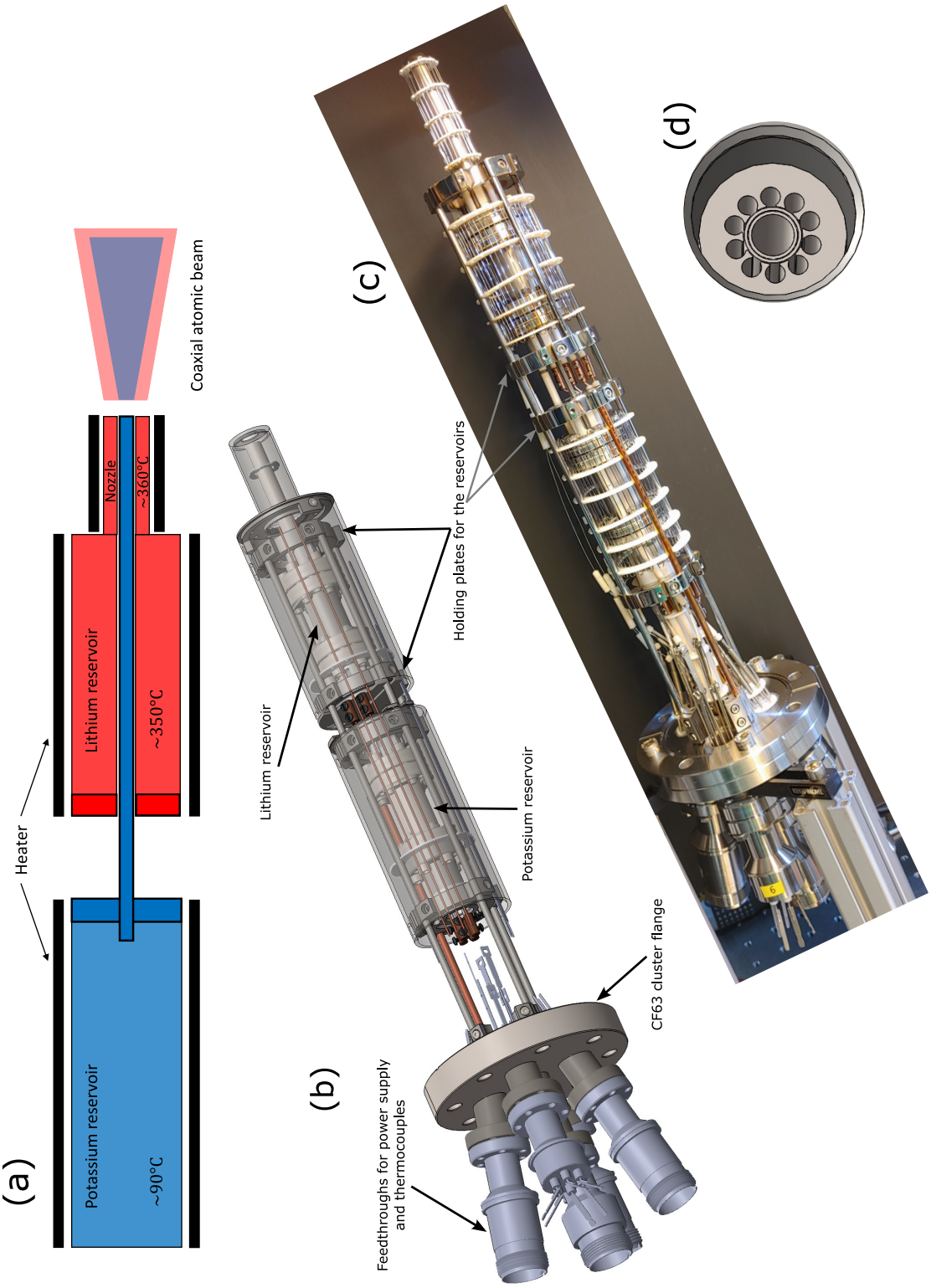

Figure 3.1: The new oven for FeLiKx. In (a): A schematic drawing of the general idea to have the two reservoirs behind each other resulting in a coaxial output. In (b): The *SolidWorks* rendering of the oven mounted on a CF63 cluster flange with feedthroughs for power supply and temperature sensors. In (c): A picture of the finished oven without heatshields. In (d): A front view of the oven output with the K tube surrounded by the ten Li tubes. The whole oven is placed inside vacuum.

3.2 New design

General idea Today a common possibility in the field is to buy a commercial oven[1]. But the standard products offered do not satisfy several of our requirements. Mostly, they are designed for one species only or for two species evaporated at similar temperatures and their efficiency is not ideal. So we had to switch to a home-built solution. A schematic drawing introducing our general idea of the new oven is shown in Fig. 3.1(a). The reservoirs in which the atoms are stored and evaporated are located behind each other with potassium at the back. The potassium atoms emerge from their reservoir through a tube that passes through the center of the lithium reservoir and the lithium atoms exit through ten smaller tubes evenly spaced around the potassium tube such that a coaxial nozzle is generated as can be seen in Fig. 3.1(d). Both reservoirs and the nozzle are surrounded by heating filaments sitting as close as possible for efficient heating. The decision to have potassium at the back and lithium at the front is due to the higher melting point of lithium. Both reservoirs are standard CF16 full nipple pipes with a length of 44 mm for Li and 48 mm for K, respectively. They are closed with custom made flanges on which the tubes are welded. Since alkalis react with copper, the gaskets we use have to be made from nickel to be safe from being corroded.

In Fig. 3.1(b) the *SolidWorks* rendering of the oven is shown. Here one can clearly see its three major sections: the K reservoir, the Li reservoir and the nozzle. For us, an important aspect for a new design is the easy detachability of the oven from the vacuum chamber and a composition that can be fully disassembled. Thus, its base is a CF63 cluster flange with five CF16 ports. Mounted on this flange in a circle with radius 23 mm there are three holding rods made from stainless steel with a length of 320 mm each. These rods serve as the skeleton for the oven, so to speak, since the reservoirs are going to be threaded on them. To fasten the positions of the reservoirs along the rods we manufacture holding plates being put in front and behind them. Detaching the base flange therefore enables us to remove the entire oven from the vacuum. The five CF16 ports are used for vacuum feedthroughs to support the oven with power and to connect temperature sensors. The two reservoirs and the nozzle are covered with heat shields that are semitransparent in the rendering. Figure 3.1(c) shows a picture of the assembled oven. The heat shields are not mounted yet in order to provide better insight.

Temperature control The most straightforward requirement is the temperature range the oven is supposed to be operated in. In Fig. 3.2 the vapour pressure curves for both elements in the liquid state are plotted. The melting point of lithium is 180.5 °C and of potassium it is 63.7 °C [Geh03; Tie09]. As the vapour pressures of the two species differ by six orders of magnitude for a fixed temperature, it is clear that the oven must provide two thermally separated regions. Via Eqs. (2.3) and (2.2) we can infer on an operating temperature for each species that sustains a desirable flux. For lithium this is around 350 °C and for potassium around 90 °C. So, in contrast to the old design, we decided to implement the heating in

[1] For example from the german distributor `www.mbe-komponenten.de`.

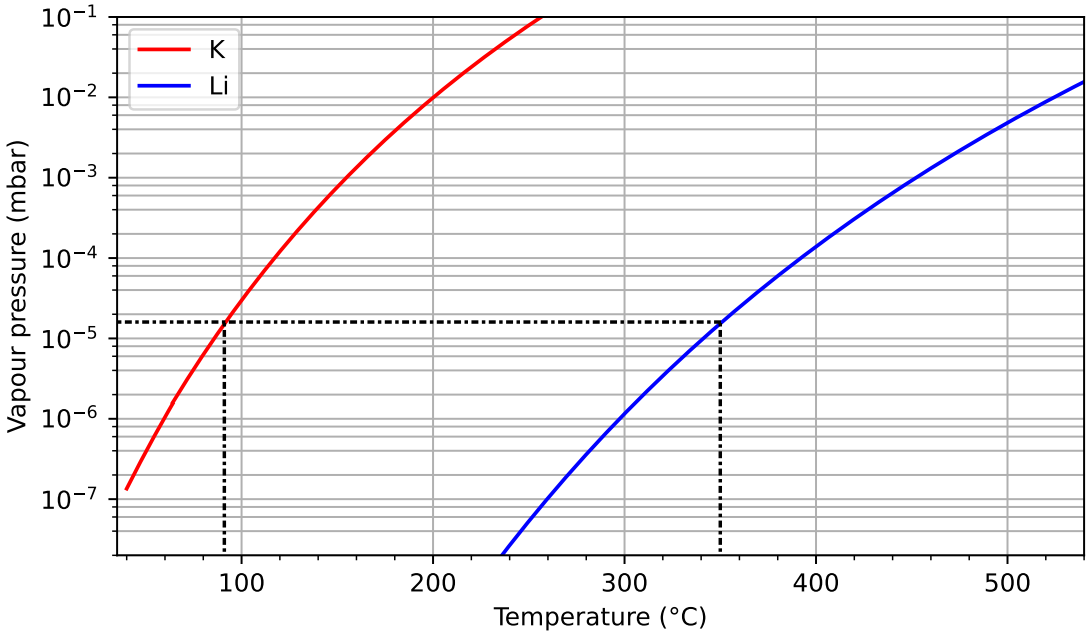

Figure 3.2: Vapour pressure curves for potassium (red) and lithium (blue) in the liquid state. The black dashdotted lines mark operating temperatures at which both elements have a sufficient flux at similar vapour pressure. The data is taken from [Alc84].

vacuum as well. This makes it easier to sustain the two thermally separated regions and is additionally more efficient than to heat the whole vacuum chamber from outside. For each of the three sections of the oven a heater was manufactured in-house. The one for the lithium section can be seen in Fig. 3.3(a), the other two are conceptually identical. They are made from a single tantalum wire formed into a cylindrical filament designed to enclose the reservoir/the nozzle coaxially. To be kept in shape they are fastened with custom made ceramic plates. At the desired operating temperatures the three heaters consume around 19 W in total.

In order to guarantee precise knowledge as well as individual control of the temperatures within the two reservoirs and at the nozzle there are seven K-type thermocouples distributed over the oven. Both of the reservoirs have a thermocouple sitting within both of their flanges and one placed at the heater right in between two windings. The red markers on the lithium reservoir in Fig. 3.3(b) clarify the two positions for the thermocouples within the flanges. Additionally there is a thermocouple in the nozzle heater. The thermocouples are guided out of vacuum via feedthroughs and get connected to a Mini8 controlling unit by *Eurotherm*. This device reads out the current temperature and acts as a proportional-integral-derivative (PID) controller for stabilization. A further advantage of heating from as close as possible is that the PID loop gets more precise since the change in temperature close to the sensor is achieved faster.

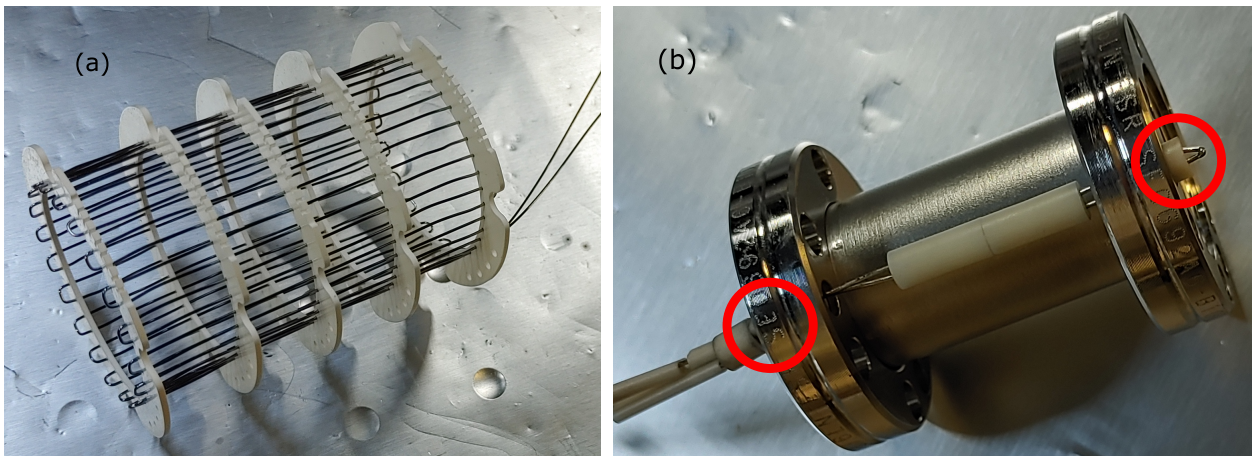

Figure 3.3: In (a): The heating filament for the lithium reservoir made from a tantalum wire kept in shape by the white ceramic plates. In (b): The lithium reservoir without its tube. The red circles mark the positions of the two thermocouples located in the front and back flange. The same positions are chosen in the potassium reservoir.

Tube aspect ratios As due to several observations we assume clogging of the microtubes due to capillary action to be a serious problem of the old oven, it is straightforward to focus efforts on preventing this scenario from happening again. To avoid wicking 'the bigger the tube diameter the better' but of course this also reduces the aspect ratio and thus, as shown in Fig. 2.4, the efficiency. In order to determine a proper aspect ratio of the tubes for both species such that ideally the source is operated at the edge of the transparent regime, it is necessary to know their mean free paths at the temperatures specified above. According to Eq. (2.6) the mean free path of the atoms depends on the collisional cross-section which can be calculated via

$$\sigma_{\mathrm{col}} = 5 \times 10^{11} \left(\frac{C_6}{\bar{v}} \right)^{2/5} \tag{3.1}$$

where C_6 is the van der Waals coefficient in $\mathrm{erg} \cdot \mathrm{cm}^6$ and $\bar{v}$ the mean atomic velocity in cm/s according to Eq. (2.28) [Sta05; Mas34]. For potassium a theoretical value for C_6 of 1630 and an experimental one of 1522 exists [Fon61; Buc65]. As the opaque regime starts with $\lambda_{\mathrm{mf}} \leq L$ we can infer on a reasonable tube length via $L_{\mathrm{K}} = \lambda_{\mathrm{mf}}(T = 90\,^{\circ}\mathrm{C}) \approx 204\,\mathrm{mm}$ depending on which value for C_6 we use. For lithium in literature there exists to our knowledge no experimental van der Waals coefficient yet. Theoretical values are 500 and 1400 and would result in a tube length of at least $L_{\mathrm{Li}} > 0.5\,\mathrm{m}$ [Fon61; Cro69].

Since we mount the reservoirs behind each other on the holding rods and the potassium reservoir has to be the rear one due to the higher vapour pressure, we can only achieve an optimal tube length for one of our species. As the fermionic isotope of potassium ^{40}K has an abundance of only 0.012 % we buy enriched samples which are expensive. Due to this, we focus on potassium when it comes to efficiency, especially since lithium is very cheap in comparison. The tube diameters should be as small as possible for a high efficiency (see Fig. 2.4). On the other side we might run into the problem of them getting clogged if

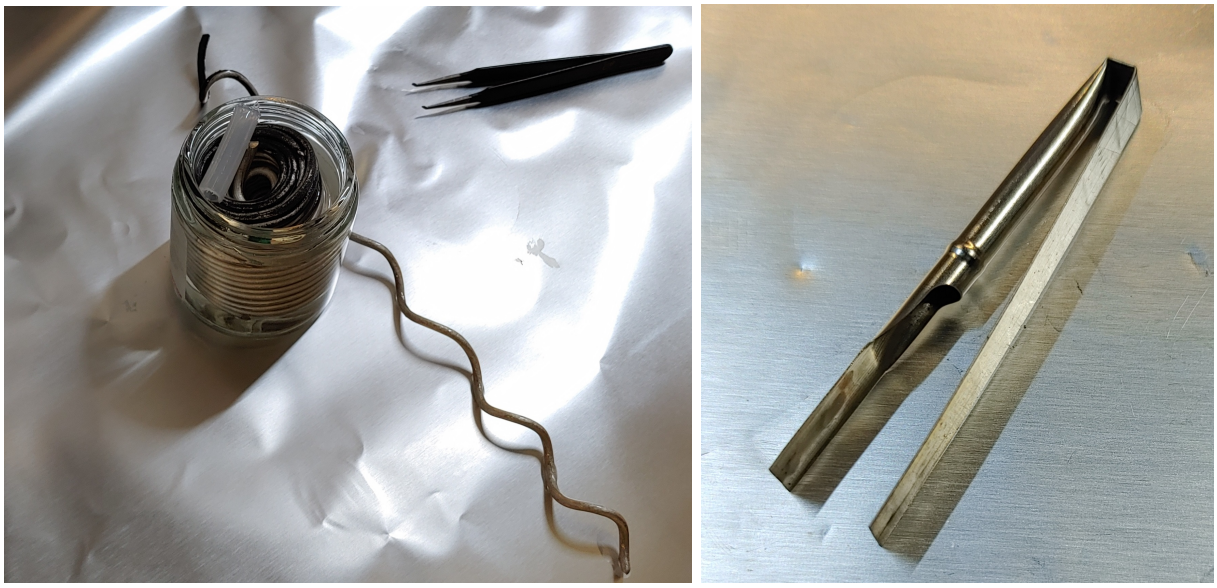

(a) (b)

Figure 3.4: (a): The jar with the mineral oil and the lithium wire inside. Next to it a piece we cut off for cleaning and packing into the steel mesh. (b): A dispenser filled with a mixture of potassium chloride and calcium powder, reacting to bare potassium via $2\,\mathrm{KCl} + \mathrm{Ca} \longrightarrow 2\,\mathrm{K} + \mathrm{CaCl_2}$.

they are too small. Eventually, for potassium there is one tube with an aspect ratio of 161 and for lithium there are ten tubes each with an aspect ratio of 139. With the chosen tubes we are perfectly on the edge of the transparent regime for potassium which is supposed to result in an atomic beam with high efficiency and simultaneously high flux. For lithium we are roughly one order of magnitude below the edge but as it is cheap, we can always simply increase its temperature to get more flux even though we loose in efficiency.

Loading In order to avoid the current, sloppy loading procedure we change to potassium stored under argon atmosphere in dispensers sealed with indium as shown in Fig. 3.4(b). Two of those dispensers get mounted into the reservoir next to each other. They can both be powered individually. During our measurements an operating current in the range between 3.4 and 4 A turned out to be useful. When first used they have to be activated with a higher current in order to make the indium seal melt. We find that the activation and operation of only one dispenser leaves the other one unaffacted even though their distance is just a few millimeters. Due to the low abundance of $^{40}\mathrm{K}$ we buy enriched samples in form of potassium chloride mixed with calcium powder. Once the dispensers get heated they emit metallic potassium via $2\,\mathrm{KCl} + \mathrm{Ca} \longrightarrow 2\,\mathrm{K} + \mathrm{CaCl_2}$. However, all measurements presented in this thesis are done with natural samples.

We buy lithium as a wire which comes in a jar with mineral oil to prevent oxidation (see Fig. 3.4(a)). In order to further prevent oxidation we execute the following steps under argon atmosphere realized by a glove-bag: We first get the lithium out of the oil, cut a piece

off and do a rough cleaning with a wipe. Next, we scratch off its surface using a knife and cut little pieces of approximately $5 \times 3 \times 2\,\mathrm{mm}^3$ which we wrap in steel meshes. Once the reservoir heats up and the lithium melts, the mesh is supposed to soak up and such confine the liquid. Additionally, we wrap the potassium tube within the lithium reservoir with mesh to prevent lithium condensing on it. Eventually, we fill the reservoir with the little lithium packages and flange it together with its lid. In order to keep lithium under argon atmosphere, we close the end of the tubes with a little plastic cap that we remove briefly before putting the oven into vacuum. If desired at some point, it is also possible to place up to six dispensers filled with lithium in the reservoir.

4 Experimental setup

In this chapter the experimental setup for taking the transverse spectra and measuring the beam profile is explained. It starts with a description of the detection volume in which atoms and light interact before it proceeds to a more thorough discussion of the most important electric devices used. Here, the photomultiplier tube (PMT) detecting the flourescence and the event counter used to count the resulting electric peaks are explained. In the end we show our optical setup and the shape of the laser beam that excites the atoms.

4.1 Detection volume

In Fig. 4.1 we show the vacuum setup we use for our measurements. The whole chamber is evacuated to a pressure of roughly 9×10^{-8} mbar, depending on the temperature of the oven. Let's define our coordinate system as follows. The z-axis is equivalent with the atomic beam axis and in the plane orthogonal to it the y-axis is the vertical and the x-axis the horizontal axis just as depicted on the top left of Fig. 4.1. The oven is flanged to a port aligner by *Lesker*[2] to add two axial degrees of freedom. Onto this port aligner a full nipple pipe is flanged. Then a five-way cross equipped with CF63 viewports, that are anti-reflective coated for the resonance wavelengths of Li and K, provides optical access to the oven nozzle. The viewport on top of the cross is covered by an aluminium plate of 10 mm tickness with a hole of 32 mm diameter in its center in which a lenstube with adjustable length is placed. On top of this lenstube there is the photomultiplier tube that detects the flourescence photons emitted by the excited atoms.

After the five-way cross there is a four-way reducer-cross on which a pneumatically driven rotary feedthrough[3] is mounted. This device rotates a shutter for the atomic beam as can be seen in more detail in Fig. 4.2(a). This shutter is going to be implemented in the main experiment too and we use this setup to test its functionality. It is operated via a digital output available on the Mini8 PID that we use to control the temperatures. On the other side of the reducer-cross the pressure sensor by *Pfeiffer*[4] is mounted. Then a reducer tee follows to connect the vacuum pump. After this a cube equipped with CF63 flanges on all six sides follows. On the bottom of the cube a blind flange is mounted and on the remaining four sides viewports coated for our resonance wavelengths provide optical access. In the flange

[2]Model PA64-H; providing ±5 mm axial adjustment
[3]Model MD16A by *UHV Design*
[4]Model PKR 361

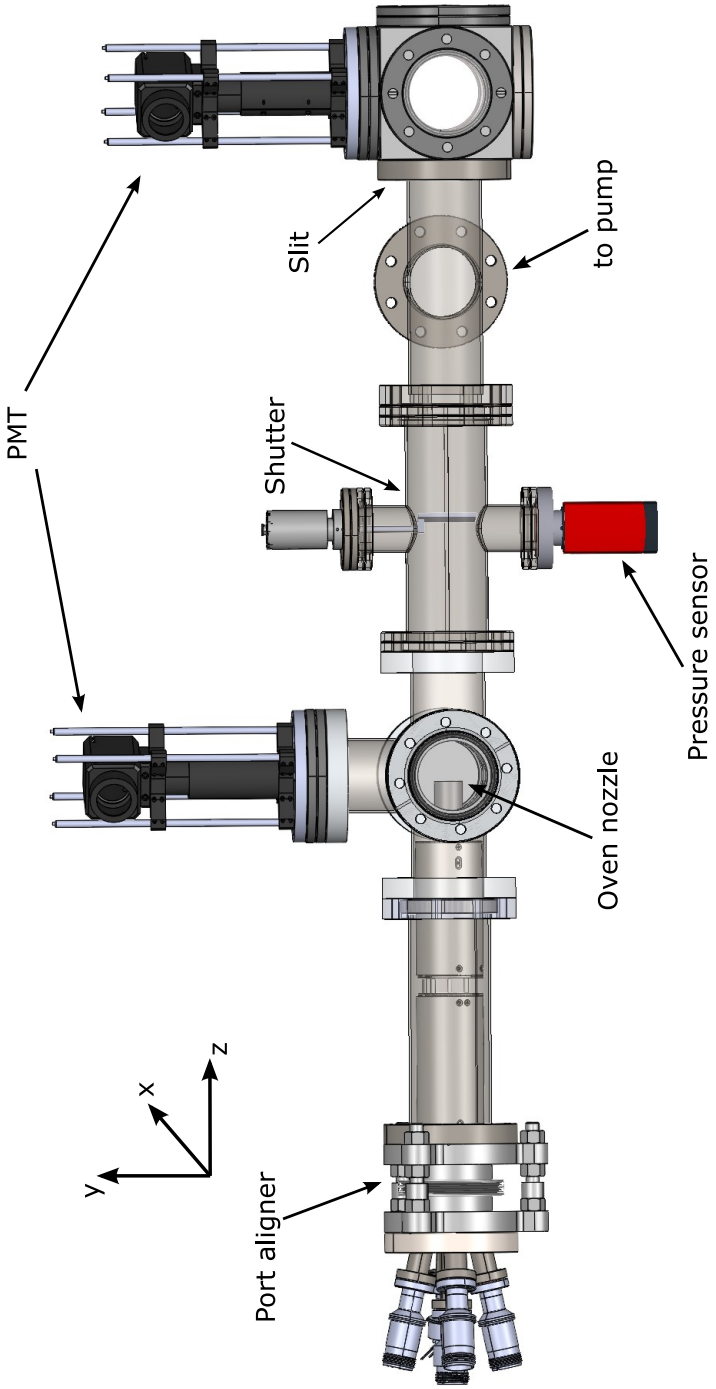

Figure 4.1: A semitransparent *SolidWorks* rendering of our measurement setup. The oven is mounted to a port aligner that adds two angular degrees of freedom. The flux measurements are executed directly after the oven nozzle. For the measurements regarding the efficiency of our oven we move the PMT to the top of the cube at the other end of the vacuum chamber and measure at this position. The beam shutter and the slit in the beam path are shown in detail in Fig. 4.2.

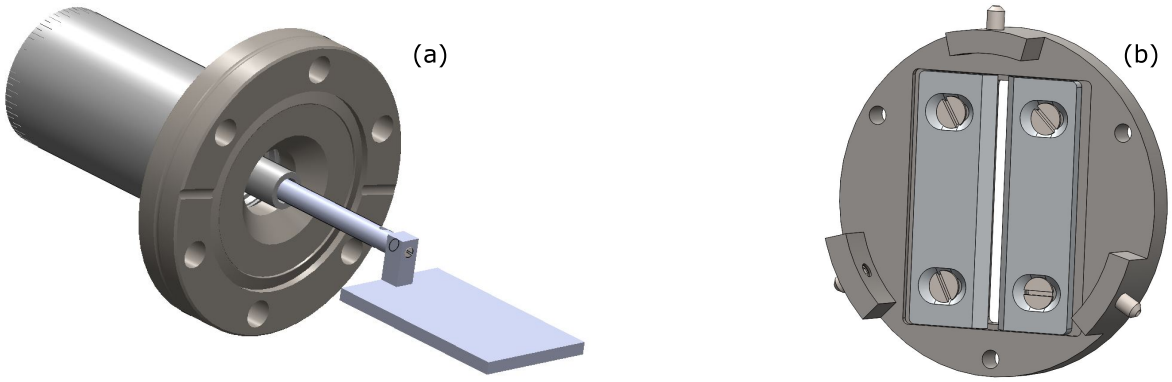

Figure 4.2: In (a): The rotary feedthrough with the shutter for the atomic beam. In (b): The slit cutting the atomic beam. Its width is adjustable via the two jaws.

between reducer cross and cube a slit, which is shown in Fig. 4.2(b), is set into the beam path just as marked in Fig. 4.1. We spread it into the flange using three M3 socket screws. Its distance to the center of the cube is 5.5(5) cm and its width is 1.0(1) mm.

Flux measurements For the measurements of the emitted atomic flux the laser beam enters the five-way cross through the viewport on the right of the atomic beam, such that it is parallel to the x-axis intersecting the atoms at 90° angle. The distance of the oven nozzle to the center of the five-way cross is 1.5(3) cm. The transverse spectra are thus taken right in front of the oven output. In this way we can capture almost all of the emitted atoms due to their small spatial expansion perpendicular to the beam axis at this position.

Efficiency measurements For the measurements regarding the efficiency of our oven the laser beam enters the cube through the viewport on the right of the atomic beam, again such that it is parallel to the x-axis. We move our PMT from the five-way cross to the cube as shown in Fig. 4.1. The distance of the oven nozzle to the center of the cube is 62(1) cm. Here we choose a larger distance in order to resolve the angular spread. As we do not capture all of the emitted atoms for these measurements due to the slit, the detected signal is thus way lower and hard to distinguish from the background. To be able to differ between background and actual signal caused by the atomic flourescence, we make use of the beam shutter which allows us to take data with and without atoms.

4.2 Photomultiplier

For the detection of the flourescence photons we use the photomultiplier tube R928P by *Hamamatsu* and drive it with a voltage of 1 kV. Its active area i.e. the area sensitive to photons has a size of $8 \times 24\,\mathrm{mm}^2$ and sits on top of a lenstube with radius 12 mm. In order to be able to precisely determine the solid angle that the active area covers, we conduct characterization measurements prior to taking any spectrum. On the one hand we alter the

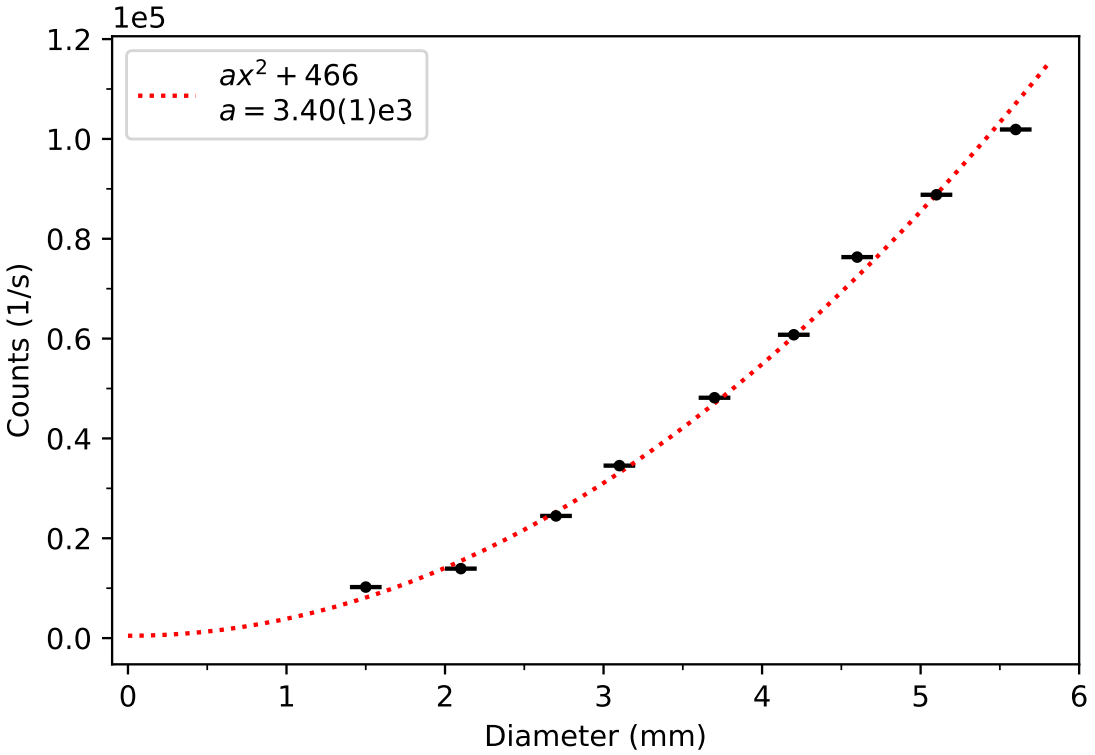

Figure 4.3: Counts per second depending on the diameter of the aperture in front of the active area. The dashed red line is a quadratic fit to the black datapoints with a fixed offset that results from the dark counts given in the datasheet of the PMT [Ham21].

distance between the PMT and the center of the atomic beam h from 240 to 360 mm, on the other hand we can change the detection area itself by inserting a circular aperture with adjustable diameter $d \in [0\,\text{mm}, 6\,\text{mm}]$ directly in front of it. The solid angle covered by the sensitive area equals

$$\Omega = \int_0^{2\pi} \int_0^{\theta} \sin(\theta')\, \mathrm{d}\theta'\, \mathrm{d}\phi = 2\pi\,(1 - \cos\theta)\,, \tag{4.1}$$

with the opening angle $\theta = \arctan(d/2h)$. Thus, for the dependence of the signal on the diameter of the aperture d we expect an quadratic behaviour $\propto d^2$ and on the distance h to the atoms an inverse quadratic behaviour $\propto h^{-2}$.

In our first measurements varying the diameter of the aperture we are not able to see this expected behaviour. Instead, the signal seems to be linear in d. We amount this to stray light reflected on the inside of the vacuum chamber that enters the PMT from large angles. To suppress these additional unwanted photons we distribute three more apertures evenly into the lenstube effectively reducing its radius to 6 mm. The data taken with this improved lenstube setup is plotted in Fig. 4.3. It shows the signal over the diameter of the sensitive area, which is adjusted by the aperture in front of it. Now the red dashed quadratic fit clearly

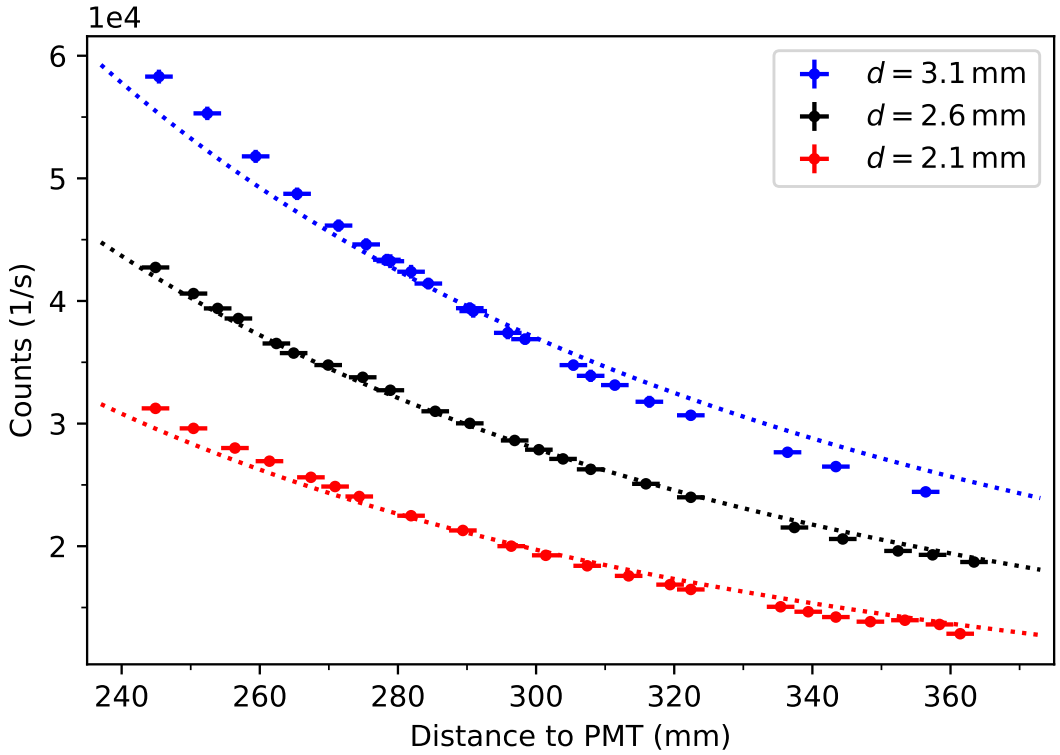

Figure 4.4: Counts per second depending on the distance of the PMT to the atomic beam. The colors correspond to three different effective sizes of the sensitive area with diameter d. The dashed lines are inverse quadratic fits ($\propto x^{-2}$) to the respective datapoints.

indicates that the datapoints reproduce the expected behaviour. The fixed offset of the fit function is due to the dark counts of the PMT noted in its datasheet [Ham21].

Regarding the distance to the atomic beam, Fig. 4.4 shows data for three different aperture diameters. The dotted lines are the respective fits according to $y(h) = c/h^2$ with free parameter c. Notable is that for all three data sets the points for small distances deviate upwards. Again, we strongly assume that, due to the increased angle under which light can reach the PMT for smaller distances, this effect can be attributed to stray light. The deviations from the fit are the smallest for the data with $d = 2.6\,\text{mm}$ and the largest for $d = 3.1\,\text{mm}$. The points nevertheless follow the quadratic behaviour in all three cases. One further has to note that the datapoins only represent the wing of the function for comparable large distances. Due to the setup, however, we are not able to adjust smaller distances with $d \leq 240\,\text{mm}$. In the end we decide for a diameter $d = 2.6\,\text{mm}$ and a distance $h = 270\,\text{mm}$ for all further measurements.

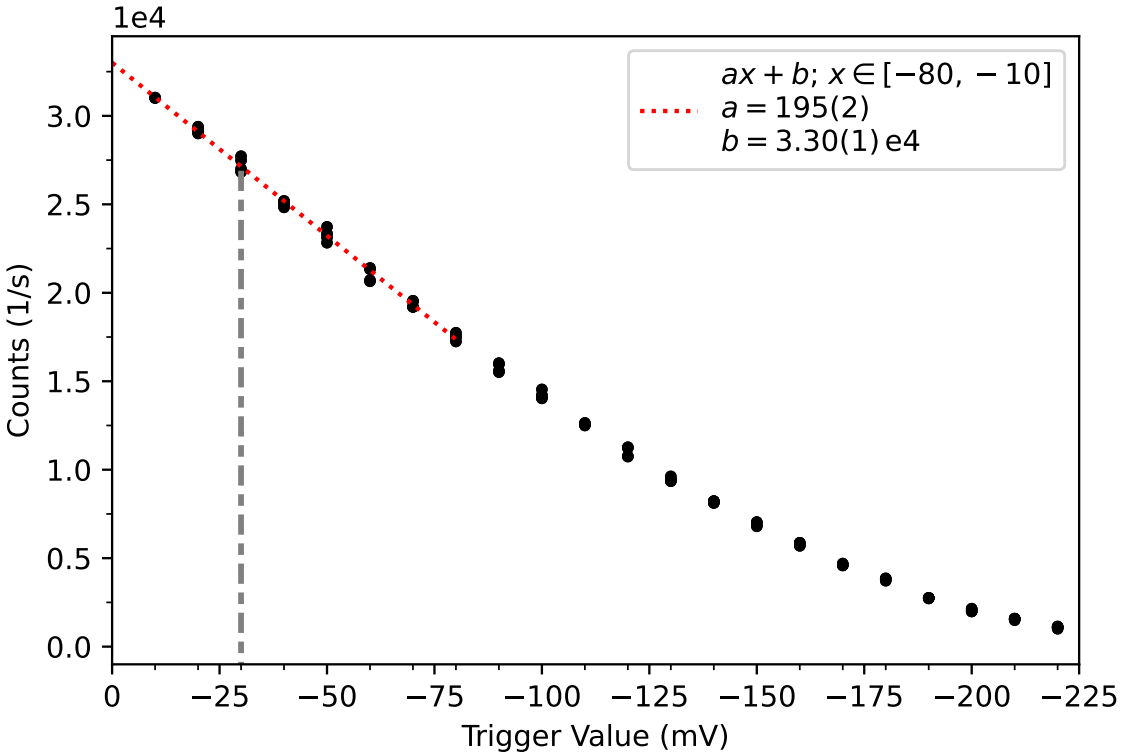

Figure 4.5: Counts per second depending on the trigger value of the event counter. The dotted red line is a linear fit to the datapoints in the interval $[-10\,\mathrm{mV}, -80\,\mathrm{mV}]$ extrapolated to zero. The dashed gray line marks our choice for the trigger value of $-30\,\mathrm{mV}$ for all further measurements.

4.3 Event counter

From the output signal of the PMT we split off the DC component, amplify the RF component and add a 140 MHz low-pass filter before guiding it to the frequency and event counter SR620 by *SRS*. This device is able to count electric pulses within an adjustable time interval and automatically averages over $x \in [1, 10^5]$ samples. The main setting is its trigger value that can be adjusted in steps of $\pm 10\,\mathrm{mV}$ and which determines the minimum amplitude an electric pulse must have in order to be counted. If we set this trigger value to 0 mV we measure a lot of noise in the signal additionally to the counts that are due to detected photons. Thus, the counts get an artificial offset. In order to circumvent this problem we examine the PMT pulses on an oscilloscope and decide on a reasonable trigger value of $-30\,\mathrm{mV}$ (the single photon pulses have a negative amplitude).

Of course, in this way we generate a systematic error as we neglect all pulses with an amplitude smaller than $-30\,\mathrm{mV}$. To compensate for this deviation we measure the counted pulses depending on the trigger value, which is shown by the black datapoints in Fig. 4.5. The dotted red line is a linear fit to the data in the interval from -10 to $-80\,\mathrm{mV}$ extrapolated to 0 mV. Now we compare the measured counts at our chosen trigger value of $-30\,\mathrm{mV}$, which is

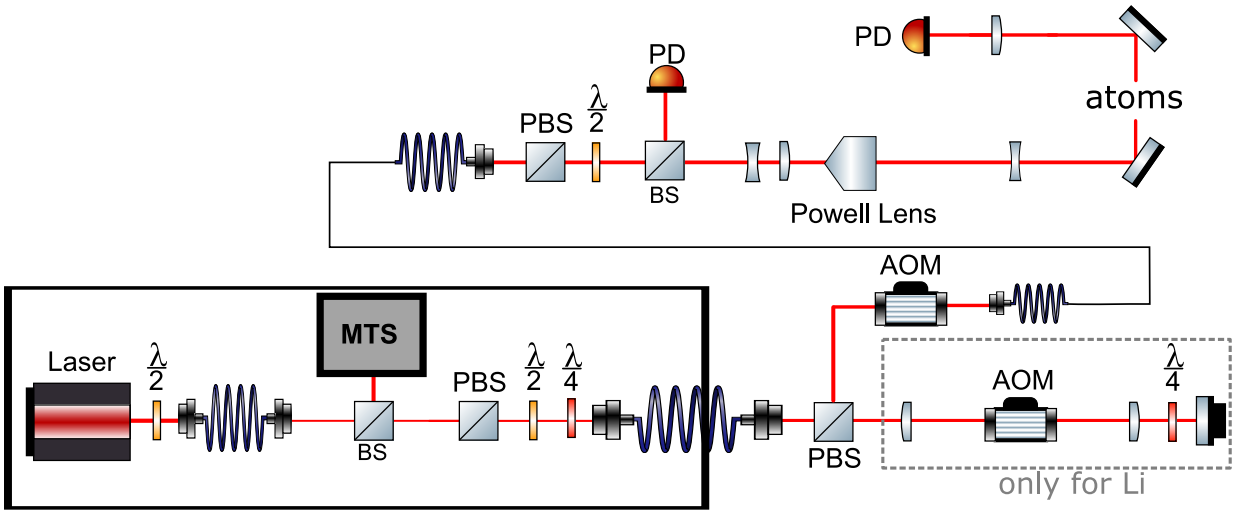

Figure 4.6: The optical setup for the measurement of the transverse spectra behind the oven nozzle. The laser is locked via modulation transfer spectroscopy. The double-pass and single-pass acousto-optic modulators compensate for the offset from the lock and the Powell lens creates a homogenous vertical beam profile. With the two photodiodes we can check if the amount of absorption of the laser light is negligible.

represented by the dashed gray line, with the extrapolated counts at 0 mV. This results in a factor of $2.72(3)/3.30(1) = 0.82(1)$, which means that we loose about 18 % of the actual counts. This factor is important later on for the quantitative measurements of the emitted flux.

4.4 Optical setup

Flux measurements In Fig. 4.6 the optical setup we use to measure the emitted flux is shown schematically. Both lasers (Li & K) are locked with a frequency offset below resonance by modulation transfer spectroscopy (MTS). This offset of 480 MHz for lithium is compensated by the double-pass (DP) and single-pass (SP) acousto-optic modulator (AOM). For potassium we omit the double-pass AOM as the shift only amounts to 208 MHz. After that a polarizing beam splitter (PBS) for polarization-cleaning is used. A fraction of the power is directed via a beamsplitter (BS) to a photodiode (PD) that we use to measure the laser power. Regarding the horizontal direction the beam is widened to approximately 2 mm by a combination of two cylindrical lenses. As we want to excite all emerging atoms with the same light intensity we make use of a Powell lens followed by a cylindrical lens to create a homogenous intensity distribution in the vertical direction. Then the beam enters the vacuum chamber where it intersects the atomic beam at 90° angle. On the other side of the 5-way cross we focus the beam into a second photodiode in order to see if absorption might play a role in the measurements.

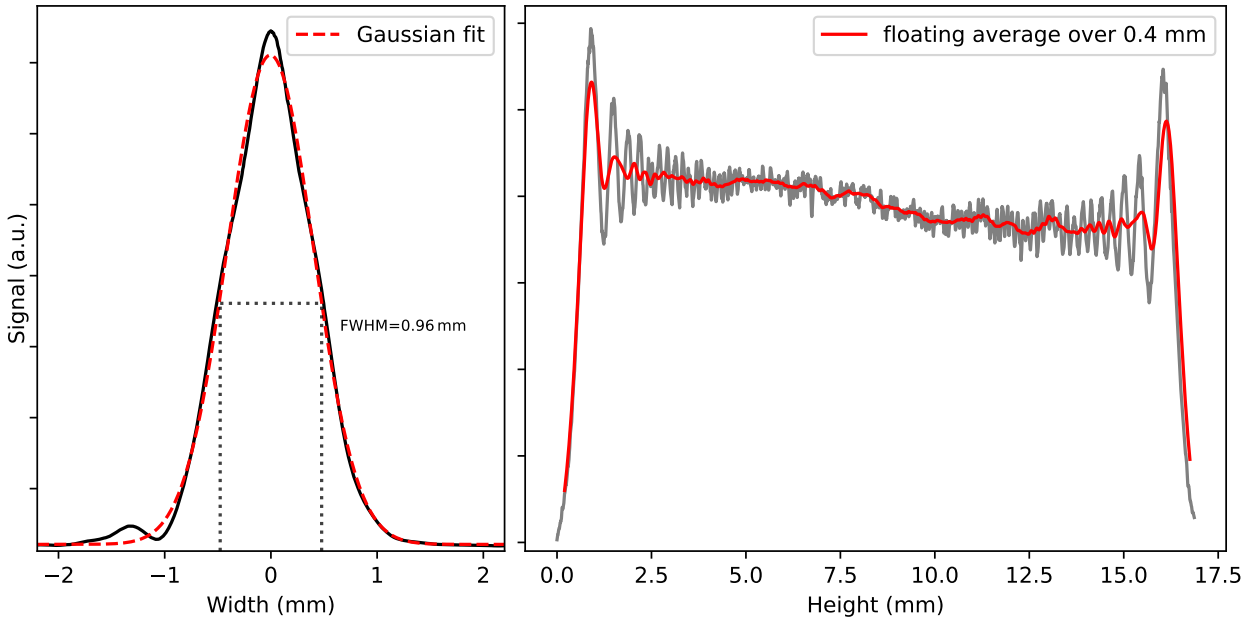

Figure 4.7: The profile of the laser beam used to excite the atoms in the measurement for the determination of the total flux. The left plot corresponds to the horizontal axis, the right plot to the vertical axis.

The intensity profiles for both axes are shown in Fig. 4.7, with the left side corresponding to the horizontal direction and the right side to the vertical one. As expected, the horizontal profile basically follows a Gaussian distribution with an exception on the left wing, where one can see a small second peak with an amplitude of roughly six percent compared to the main peak. We do not further care about this deviation as for the later calculations the exact intensity distribution along the horizontal axis does not matter. Along the vertical axis we can see that on the upper and lower end the intensity is clearly higher than in the middle where it is rippled. This is the typical behaviour of a Powell lens and we expect to see this. The red line is a floating average over 0.4 mm of the original data and shows that even without the edges the profile is not totally flat in the middle. For larger values along the axis between 10 and 15 mm the intensity is about ten percent less than for smaller values between 2.5 and 7.5 mm. Since this deviation from an ideal flat distribution is only small, we neglect it and assume a constant power along the beam height.

Efficiency measurements For the measurement of the atomic beam shape the optical setup is similar to the one shown in Fig. 4.6. For potassium we switch as well to a double-pass AOM for the compensation of the frequency offset due to the lock. This enables us to compensate small frequency drifts by simply changing the AOM frequency. Now the beam is supposed to be Gaussian along both axes, which is why the modifications are the following: After the beamsplitter that feeds the PD we replace the cylindrical lenses and the Powell lens by a telescope configuration of two spherical convex lenses in order to adjust the beam diameter to

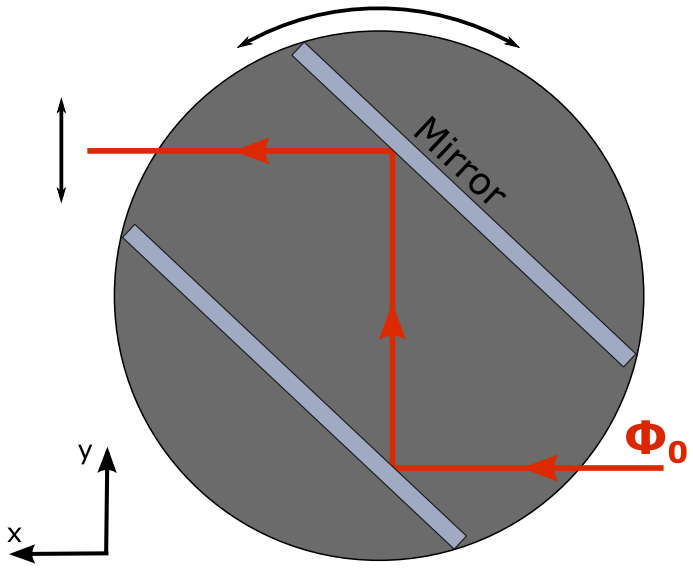

Figure 4.8: Schematic of the platform that enables us to vertically move the laser beam. The light comes from the right and gets reflected on both mirrors. As the mirrors are fixed to the rotating platform, they shift the laser beam along the y-axis.

3 mm. For an easier control of the power we additionally insert a combination of a half-wave plate and a second PBS. Then, the beam gets reflected into the vacuum chaber by a mirror. In order to move the beam up and down along the y-axis we make use of a programmable rotation stage[5]. We screw a platform parallel to the x-axis onto the rotation stage. On top of this platform we mount two rectangular mirrors, each 95 mm long and 22 mm high, parallel to each other with a distance of 97 mm. In this way when we rotate the stage both mirrors get rotated in the same way. A schematic drawing of this setup is shown in Fig. 4.8. The laser beam comes from the right and gets reflected by both mirrors such that its height can be shifted by their rotation. The big advantage is that the beam always stays prallel to the x-axis. This allows us to exclusively excite atoms that emerge the oven under a certain angle ϑ, while ϕ is already fixed by the slit.

[5]Model DRTM40 by *Owis*

5 Flux measurements

In the measurements shown in this chapter we investigate the transverse spectra of both atomic species right behind the oven nozzle. The goal is on the one hand to evaluate the data such that a quantitative statement about the total flux emitted can be made and a comparison to theory can be drawn. In the second place the spectra deliver information on the velocity distribution orthogonal to the beam axis, which is essential for the transversal cooling section that will be implemented after the oven in order to further collimate the atomic beam.

5.1 Total flux

Of course one can qualitatively compare the transverse spectra with the theoretical prediction by means of the halfwidth of the peaks or the relative height towards each other. But also a quantitative statement can be obtained once we calculate the relation of the number of measured PMT counts to the total flux causing this amount of flourescence. Therefore we start with the number of atoms N being in a volume with cross section A and thickness Δz at a certain time. We can express this number of atoms via their density n and also substitute the thickness of the volume by the product of their mean velocity $\bar{v}$ and the time Δt

$$N = nA\Delta z = nA\bar{v}\Delta t. \tag{5.1}$$

Hence the flux through the cross section is $\dot{N} = nA\bar{v}$ and the flux through the whole cross sectional area covered by the incident light is given by

$$\dot{N} = \bar{v} \iint_{-\infty}^{+\infty} n(x, y, z)\ \mathrm{d}x\,\mathrm{d}y. \tag{5.2}$$

The mean velocity of the atoms is derived from their normalized velocity distribution depending on their temperature and mass according to Eq. (2.29).

The incident light from the laser can be expressed by its photon flux and its shape. The photon flux is given by $\Phi_0 = P/(h\nu)$ where P is the power of the light, ν its frequency and h the Planck constant. This photon flux is spatially distributed according to a normalized Gaussian $G_z(z)$ in z-direction. In vertical direction we assume it to be evenly distributed with an amplitude of $1/l$ where l is the height of the beam (see also section 4.4). In this way the integration along y and z equals unity. So we can write

$$\Phi(y, z) = \Phi_0 \times \frac{1}{l} \times G_z(z). \tag{5.3}$$

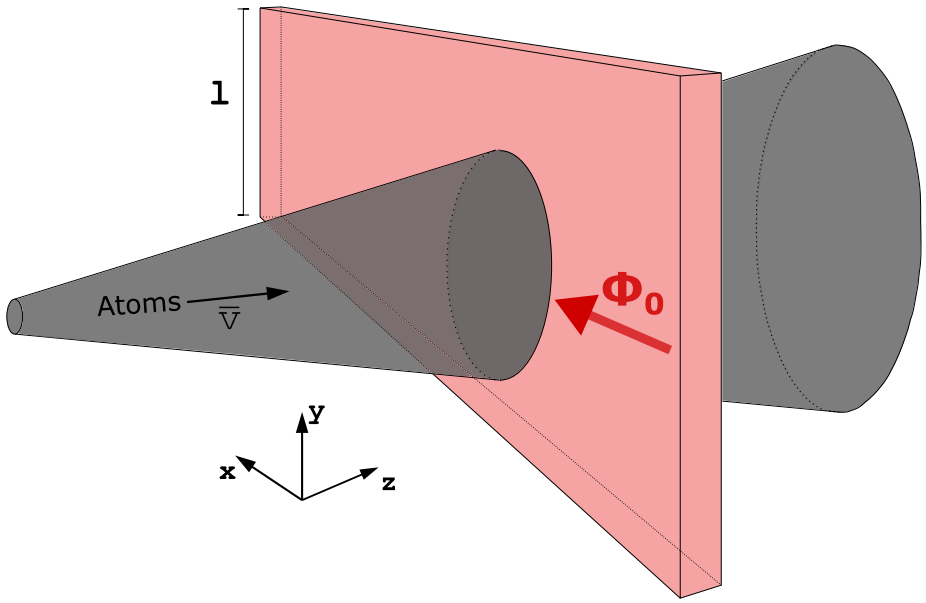

Figure 5.1: Schematic sketch of the interaction between atoms and laser light for the measurement of the total flux. The atoms move to the right along the z-axis with a velocity of $\bar{v}$. The red laser light with with photon flux Φ_0 moves along the x-axis intersects the atoms at 90° angle. For the discussion of the spatial profile of the laser see section 4.4.

As the number of flourescence photons per unit time Φ_F is proportional to the density of the atoms, their absorption cross section σ_abs and the incoming photon flux Φ we can start calculating with

$$\mathrm{d}\Phi_\mathrm{F} = n(x,y,z) \times \overbrace{\sigma_\mathrm{abs} \times \Phi(y,z)}^{R} \,\mathrm{d}V. \tag{5.4}$$

The product of absorption cross section and photon flux corresponds to the rate R at which atoms scatter photons. By further taking into account the dependence of σ_abs on the frequency ν of the incident light and on the velocity v of the atoms we get

$$\Phi_\mathrm{F} = \iiint_V \mathrm{d}V \int_\nu \mathrm{d}\nu \int_v \mathrm{d}v \; n(x,y,z)\, F(v)\, \frac{\Phi(y,z)}{(\delta\nu)}\, \sigma_\mathrm{abs}(\nu - \nu_\mathrm{D}(v)), \tag{5.5}$$

where $F(v)$ is the normalized velocity distribution of the atoms according to Eq. (2.29). The factor $(\delta\nu)$ is the discrete stepwidth we scan the frequency with. Plugging Φ from Eq. (5.3), the integral over the density from Eq. (5.2) and knowing that $G_z(z)$ is normalized we arrive at

$$\Phi_\mathrm{F} = \frac{\dot{N}}{l\bar{v}} \underbrace{\int_{-\infty}^{+\infty} G_z(z)\,\mathrm{d}z}_{=1} \int_\nu \mathrm{d}\nu \int_v \mathrm{d}v \; F(v) \frac{\Phi_0}{(\delta\nu)} \sigma_\mathrm{abs}(\nu - \nu_\mathrm{D}(v)). \tag{5.6}$$

Next, we need to calculate the absorption cross section, for which we can start with the absorption rate

$$R_{12} = \frac{|e\vec{r}_{21}\hat{\varepsilon}E_0/\hbar|^2 A_{21}/4}{4\pi^2(\nu_{21}-\nu)^2 + (A_{21}/2)^2} \tag{5.7}$$

derived from the population rate equations of the density matrix elements [Mil88]. Here e is the charge of the electron, $\hat{\varepsilon}$ is the polarization of the incident light, E_0 its amplitude, ν its frequency, ν_{21} the frequency of the atomic transition and A_{21} the spontaneous emission rate also known as Einstein A coefficient, which equals the inverse lifetime τ of the excited state. As the absorption rate equals the absorption cross section times the photon flux, we can further write

$$\sigma_{\text{abs}} = \frac{R_{12}}{\Phi} = \frac{h\nu_{12}R_{12}}{\frac{1}{2}c\varepsilon_0 E_0^2} = \frac{4\pi^2\nu_{21}D^2}{\varepsilon_0 hc}\frac{A_{21}/2}{4\pi^2\Delta^2 + (A_{21}/2)^2} \tag{5.8}$$

with $\Delta = \nu_{21} - \nu$ the detuning of the incident light from the atomic transition frequency and $\vec{D}$ the dipole moment of the transition. This dipole moment can be expressed in terms of the spontaneous emission rate by [Mil88]

$$A_{21} = \frac{D^2(2\pi)^4\nu_{21}^3}{3\pi\varepsilon_0 hc^3}. \tag{5.9}$$

Using this relation to substitute the dipole moment yields

$$\sigma_{\text{abs}} = \frac{3\pi c^2 A_{21}}{4\pi^2\nu_{21}^2}\frac{A_{21}/2}{4\pi^2\Delta^2 + (A_{21}/2)^2} = \frac{3\lambda^2}{4\pi}\frac{A_{21}^2}{2}\frac{1/4\pi^2}{\Delta^2 + (A_{21}/4\pi)^2}. \tag{5.10}$$

For light on resonance

$$\sigma_{\text{abs}}(\nu = \nu_0) = \frac{3\lambda^2}{2\pi} \equiv \sigma_0, \tag{5.11}$$

which we call σ_0 and which represents the maximum value of the absorption cross section. Rewriting the expression for σ_{abs} simplifies things as we can extract a normalized Lorentzian lineshape $L(\nu)$

$$\sigma = \sigma_0\frac{A_{21}^2}{4}\frac{(2\pi)^{-2}}{\Delta^2 + (A_{21}/4\pi)^2} = \sigma_0\frac{A_{21}}{4}\frac{(A_{21}/4\pi)(1/\pi)}{(\nu-\nu_0)^2 + (A_{21}/4\pi)^2} = \sigma_0\frac{A_{21}}{4}L(\nu). \tag{5.12}$$

At last, we can substitute the spontaneous emission rate A_{21} with the natural linewidth Γ as they are equal.

Using this expression and adding it to our integral we are left with the convolution of the velocity distribution and the Lorentzian of the absorption cross section

$$\Phi_{\text{F}} = \frac{\dot{N}\sigma_0\Gamma\Phi_0}{4l\bar{v}(\delta\nu)}\int_0^\infty\int_0^\infty F(v)\,L(\nu - \nu_0 - \frac{kv}{2\pi})\,\mathrm{d}v\,\mathrm{d}\nu, \tag{5.13}$$

where $\nu_{\text{D}} = \nu_0 - {}^{kv}/_{2\pi}$ is the Doppler shift. Since both the velocity distribution and the Lorentzian are normalized and we integrate over all velocities as well as over all frequencies,

these two integrals equal unity. Eventually, we arrive at our equation for the atomic flux determined by the measured number of flourescence photons:

$$\Phi_\mathrm{F} = \frac{\dot{N}\sigma_0\Gamma\Phi_0}{4l\bar{v}(\delta\nu)} \qquad \Longleftrightarrow \qquad \dot{N} = \frac{4l\bar{v}(\delta\nu)\Phi_\mathrm{F}}{\sigma_0\Gamma\Phi_0}. \tag{5.14}$$

Nevertheless one still has to take corrections into account when evaluating Φ_F from the obtained data. First, the PMT does not cover the full solid angle of 4π. With the chosen distance of the PMT and the diameter of the aperture in front of it (see section 4.2) we only cover a solid angle of $7.3(6) \times 10^{-5}\,\mathrm{sr}$, such that we only capture $5.8 \times 10^{-4}\,\%$ of the scattered photons. Second, the PMT has a certain quantum efficiency of detecting a photon with a given wavelength. For $\lambda = 670\,\mathrm{nm}$ this efficiency is $6.84\,\%$, for $\lambda = 770\,\mathrm{nm}$ it is $3.15\,\%$ [Ham21]. Third, we only count peaks that exceed our chosen trigger value of $-30\,\mathrm{mV}$ (see section 4.3), which means we loose about 18% according to the data shown in Fig. 4.5. From these three contributions we get an additional factor

$$\xi = \frac{7.3(6) \times 10^{-5}\,\mathrm{sr}}{4\pi} \times \eta_\mathrm{PMT} \times 0.82(1) \tag{5.15}$$

by which we have to divide the flourescence photons Φ_F.

5.2 Lithium

Figure 5.2 shows the energy levels for both lithium isotopes ^{6}Li (fermionic) and ^{7}Li (bosonic). As we use light from a *M2* laser system that is locked to the D2-line (F=3/2 → F'=5/2) of ^{6}Li via MTS during daily operation, we choose to scan around this transition for the transverse spectra. But as the D1-line of ^{7}Li is only 481 MHz away we can not avoid to also measure a signal from this transition. In total we expect our signal to be the sum of six peaks [San11; Wal03]. Four peaks are due to the ^{7}Li D1-line as both its ground and excited state have a sufficiently large hyperfine splitting (803.5 MHz & 92.03 MHz), which make it possible to individually resolve these transitions indicated by the green arrows in Fig. 5.2. Two further peaks come from the ^{6}Li D2-line. Here the excited $2\,^2\mathrm{P}_{3/2}$ state has only a small hyperfine splitting that is not resolvable in the spectra. The ground state nevertheless exhibits a splitting of 228.2 MHz, which is easily resolvable, and the respective transitions are indicated by the violet arrows in Fig. 5.2. In addition, it must be noted that the abundance of ^{6}Li is only 7.6 % and in the signal those two transitions will therefore be way less pronounced than the ones from ^{7}Li [Wil09]. Two pictures of flourescent lithium atoms in front of the oven output are shown in Fig. 5.3. The left panel is a front view of the oven nozzle, the atoms thus travel towards you. One can clearly distinguish the ten individually formed beams. The right panel is a top view where the atoms get emitted to the left.

The method of acquiring the data is as follows: First we set the desired temperature at the Mini8 PID and wait for the oven to thermalize. During this time span we already shine the laser light into the vacuum chamber and continuously track the counts of the PMT. As soon

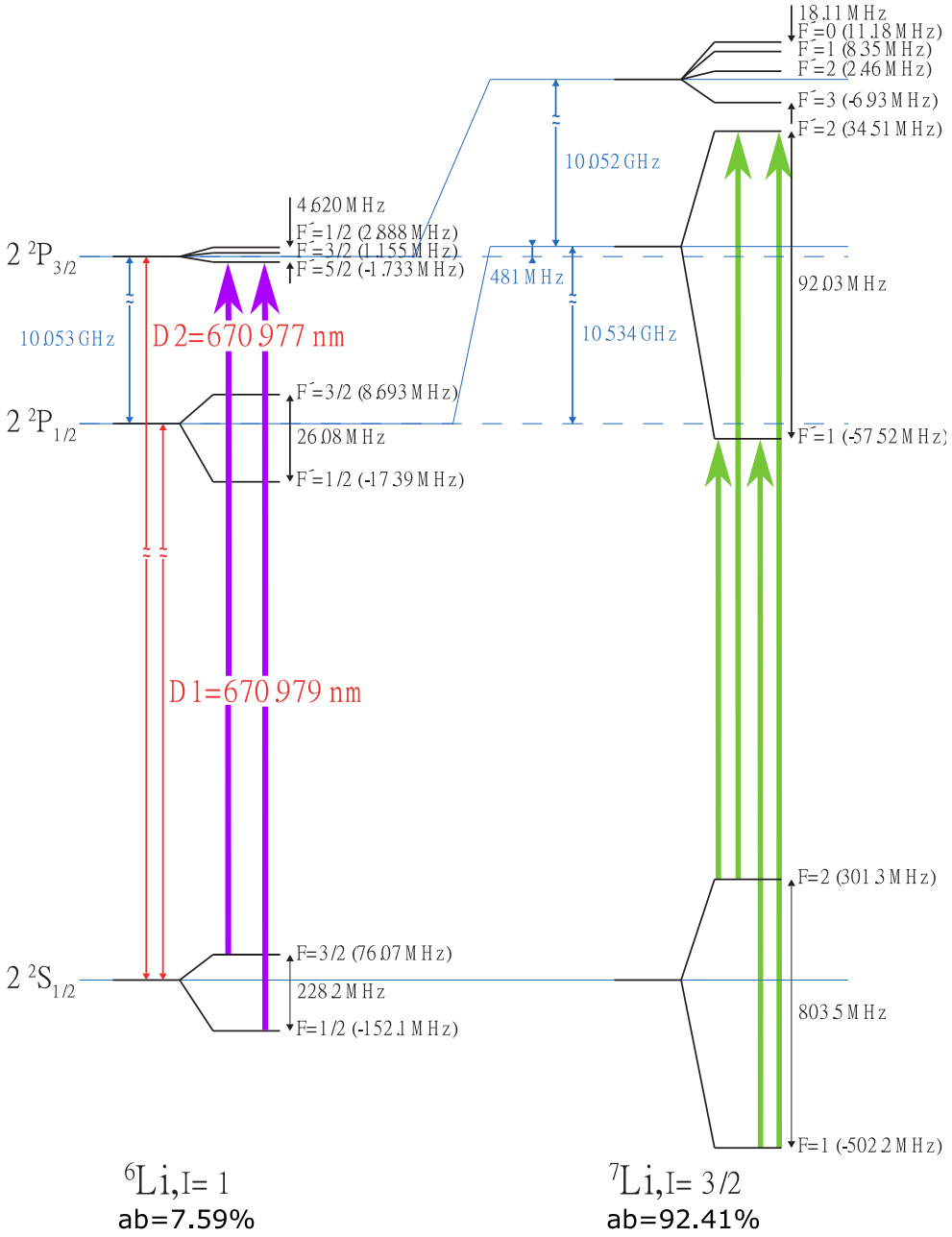

Figure 5.2: Energy levels of the D1- and D2-lines for ^{6}Li and ^{7}Li. The transitions marked in violet and green are the ones we expect to see in our spectra. The abundace of the isotopes is given at the bottom. Adapted from [Wil09].

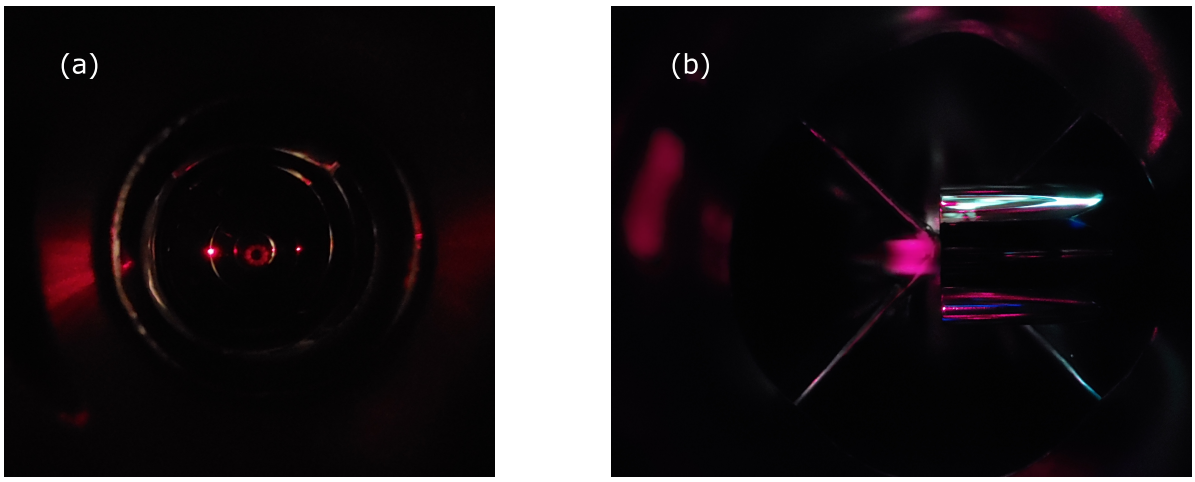

Figure 5.3: Fluorescence of lithium atoms in front of the oven output. In (a): Front view of the nozzle in which one can distinguish the ten lithium channels. In (b): Top view of the oven nozzle emitting the atoms to the left.

as they do not change anymore we assume the reservoirs to be fully thermalized and start the actual measurement. We use the USB-6008 OEM by *National Instruments* to generate an analog voltage signal that gets fed into the analog remote control input of the laser in order to scan its frequency. Simultaneously, the same device is used to log the error signal produced by the MTS. After each voltage step we record the corresponding PMT counts. The size of the frequency range we are able to scan is limited to roughly 4 GHz by two factors. First the maximum voltage signal our device can produce and second the smoothness of the laser regarding mode-hops.

The spectrum for $T = 401\,°\mathrm{C}$ corresponds to the black line in the upper panel of Fig. 5.4. The red line shows the theoretical spectrum we calculated as the sum of the individual spectra for both isotopes weighted by their abundance. This line is not calculated with an absolute amplitude and is scaled such that it overlaps with our experimental data at the peak of the ^{7}Li transitions with F=2. Its purpose is to enable us to do a qualitative analysis of the shape of our spectrum. The two individual spectra are shown as green (violet) dotted line for ^{7}Li (^{6}Li). They are calculated as the sum of all possible transitions regarding $|F, m_F\rangle \rightarrow |F', m'_F\rangle$ weighted by their probability of occupancy given by the Boltzmann factor and their transition strength given by their Clebsch-Gordan coefficients [Met99]. In total these are 108 individual possibilities for ^{6}Li and 192 for ^{7}Li. The mid panel shares the abscissa and shows the location of the transitions that contribute to the spectrum. Each transition is labeled with the angular momentum quantum number of its hyperfine groundstate (compare with Fig. 5.2). In the lowest panel the error signal is shown. It exhibits two features separated by the 228.2 MHz ground state splitting of ^{6}Li according to Fig. 5.2. The feature in the middle is the crossover signal of the two actual features on the left and right. Using this splitting we can calibrate the abscissa of the spectra taken which results in a scanning stepwidth of $\delta\nu = 3.41\,\mathrm{MHz}$.

The most distinct deviation of our experimental data from theory happens for frequencies

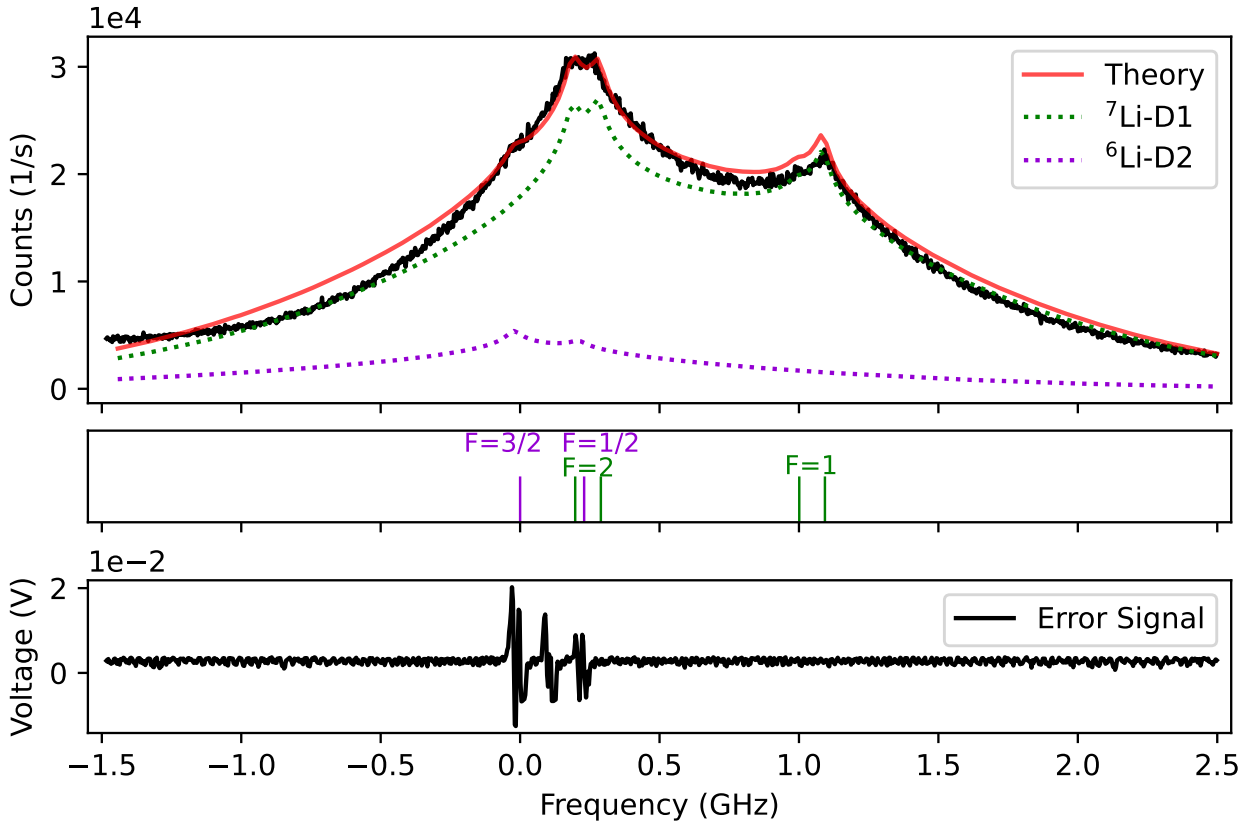

Figure 5.4: Transverse spectrum of lithium at $T = 401\,°\mathrm{C}$. In black the experimental data, in red the theoretical calculations. The green (violet) dotted line corresponds to the contribution of ^{7}Li (^{6}Li). The theoretical line is scaled such that it overlaps with the experimental data at the peak of the ^{7}Li transitions with F=2. In the mid panel the relevant transitions contributing to the spectrum are shown. The lowest panel shows the error signal used to calibrate the abscissa.

lower than roughly $-0.2\,\mathrm{GHz}$. In this range both the number of counts per second as well as the shape of the line do not match the red theory line. But also on the high frequency wing the experimental data is beneath the theory even though its shape is fitting. As the theory is not absolute it is also possible that the scaling is wrong and we detect an appropriate number of counts on the wings and too much at the peak. Against this argument speaks the fact that the atoms excited by the frequencies on the wings have a comparable high transverse velocity of up to $700\,\mathrm{m\,s^{-1}}$. This is why the points where they are resonant have an either high or low x-coordinate and the flourescence photons are not emitted in direct sight of the PMT anymore. We assume this to be the reason that we have less counts on the wings of the spectrum. Besides the points mentioned, our data qualitatively matches the theory which for us is kind of a first test if the measurements make sense.

We take spectra for several temperatures between 299 and 533 °C, where the intensity of the laser beam is always less than 3 % of the saturation intensity of the atomic transition. All of them resemble the spectrum shown in Fig. 5.4, although their amplitudes differ, of course. By integrating over the spectra we acquire the total number of detected counts. From this we

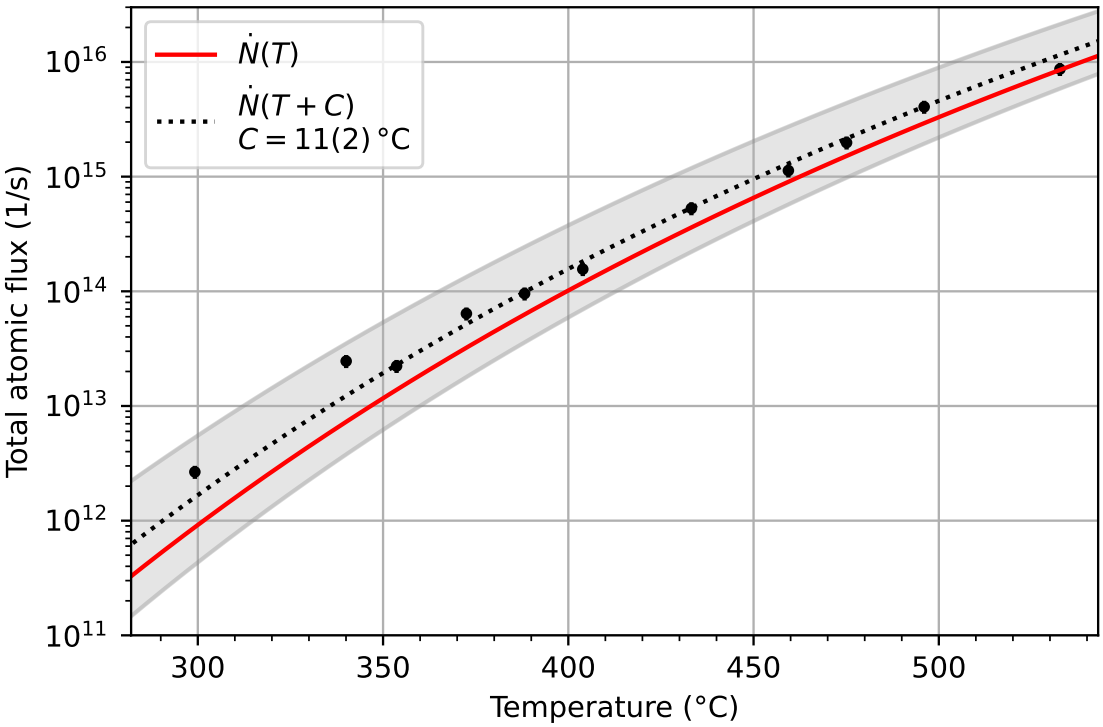

Figure 5.5: The total atomic flux of Li emitted by the oven depending on the temperature in its reservoir. The red line is the theoretical expectation and the gray area depicts the temperature uncertainty of our datapoints. The black dashed line is a fit to our data according to Eq. (2.12) where we add a free parameter C to the input temperature.

can use Eq. (5.14) from the above mechanism to calculate the total flux for each temperature. Figure 5.5 shows the total flux over the measured range of temperatures. The y-error bar indicates the systematic uncertainty in determining the total atomic flux. It is dominated by the uncertainty of the solid angle covered by the PMT (see Eq. (4.1)) resulting in a relative y-error of about 13 %. Compared to this, the error on the x-axis is rather large. For each spectrum we have two measured temperature values. One coming from the thermocouple in the front flange and one from the back flange (see Fig. 3.3). The temperature measured in the front flange is always at least 40 °C higher then the temperature measured in the back flange, which indicates that there is a temperature gradient across the reservoir. For the datapoints in the plot we use the mean temperature. The gray shaded area illustrates the uncertainty in the temperature of our datapoints due to the two thermocouple values. Additionally, one has to be aware of the uncertainty of the thermocouples themselves which is about ±2 °C. The red line corresponds to the theory according to Eq. (2.12). The black dashed line corresponds to a fit to the datapoints also according to Eq. (2.12), however with an offset C in the temperature as a free parameter that amounts to $C = 11(2)\,°C$. One can see that over the whole temperature range the theoretical curve is within the temperature uncertainty of our

datapoints. The measurements are thus in accordance with theory indicating that the lithium part of the oven indeed works as we expect, regarding its emitted flux. Remarkable is that the datapoints are closer to the theory for higher temperatures, while especially the first two points are rather on the left border of the gray temperature range.

From our measurement data we can also conclude on the time the oven is going to emit lithium before it needs reloading. At $T_{\mathrm{Li}} = 350\,^{\circ}\mathrm{C}$, which is the temperature we plan to operate the oven at, the flux according to the fit to our measurements is $1.9 \times 10^{13}\,\mathrm{s}^{-1}$. From our experience when we filled the oven we can say that an amount of 150 mg of lithium to be placed within the reservoir is reasonable. When we assume a nonstop operation 24 hours a day, seven days a week, this amount will be enough for about 21.5 years.

5.3 Potassium

For potassium the situation is a little more complex compared to lithium as we now deal with three isotopes ^{39}K (bosonic), ^{40}K (fermionic) and ^{41}K (bosonic). Here we make use of a *Toptica* laser system usually locked to the D2-line (F=2 $\rightarrow$ F'=3) of ^{39}K again via MTS. As we can see from the energy level diagram shown in Fig. 5.6, the D2-lines of ^{40}K and ^{41}K are only 125.6 MHz and 235.5 MHz away which means that our spectrum will be again the sum of several transitions from all three isotopes. For the bosonic ones the hyperfine splitting of the excited $4\,^2\mathrm{P}_{3/2}$ state is comparatively small, which is why we do not expect to see the individual transitions in the spectrum. For ^{40}K the splitting of 100.2 MHz should in principle be resolvable but its abundance is so low that we do not expect to see any contribution at all from this isotope. For the ground states the splitting is at least 254 MHz for all three isotopes resulting in an expectation of four peaks in the spectrum (neglecting ^{40}K). In contrast to lithium, here the spectrum does not contain any contribution from a D1 transition as those are roughly 1.7 THz lower in frequency. The method of acquiring the data is basically the same as for lithium in the above section. Again, the error signal produced by MTS shows two features (even though the second one is minimal) that can be used to calibrate the abscissa. In the potassium case their distance equals the ground state splitting of 461.7 MHz of ^{39}K (compare to Fig. 5.6). This results in a stepwidth of $\delta\nu = 2.12$ MHz.

In Fig. 5.7 the potassium spectrum for $T_{\mathrm{K}} = 114.5\,^{\circ}\mathrm{C}$ is shown. Similar to the lithium spectrum above, the red line corresponds to theory and the coloured dotted lines correspond to the contributions of the individual isotopes. In the mid panel the transitions contributing to the spectrum labeled with the angular momentum quantum number of their hyperfine groundstate can be seen. Here the low abundance of ^{40}K is nicely visible, as no amplitude in the theory line can be seen at the frequencies where the transitions are. The lowest panel contains the error signal. Just like for lithium the theoretical line is not calculated absolutely and is scaled such that is overlaps with the peak of the ^{39}K transition with $F = 2$. In general our data follows the expectation but for frequencies larger than 0.25 GHz it is beneath theory.

We take spectra for temperatures between 61 and 162 °C, where the intensity of the laser

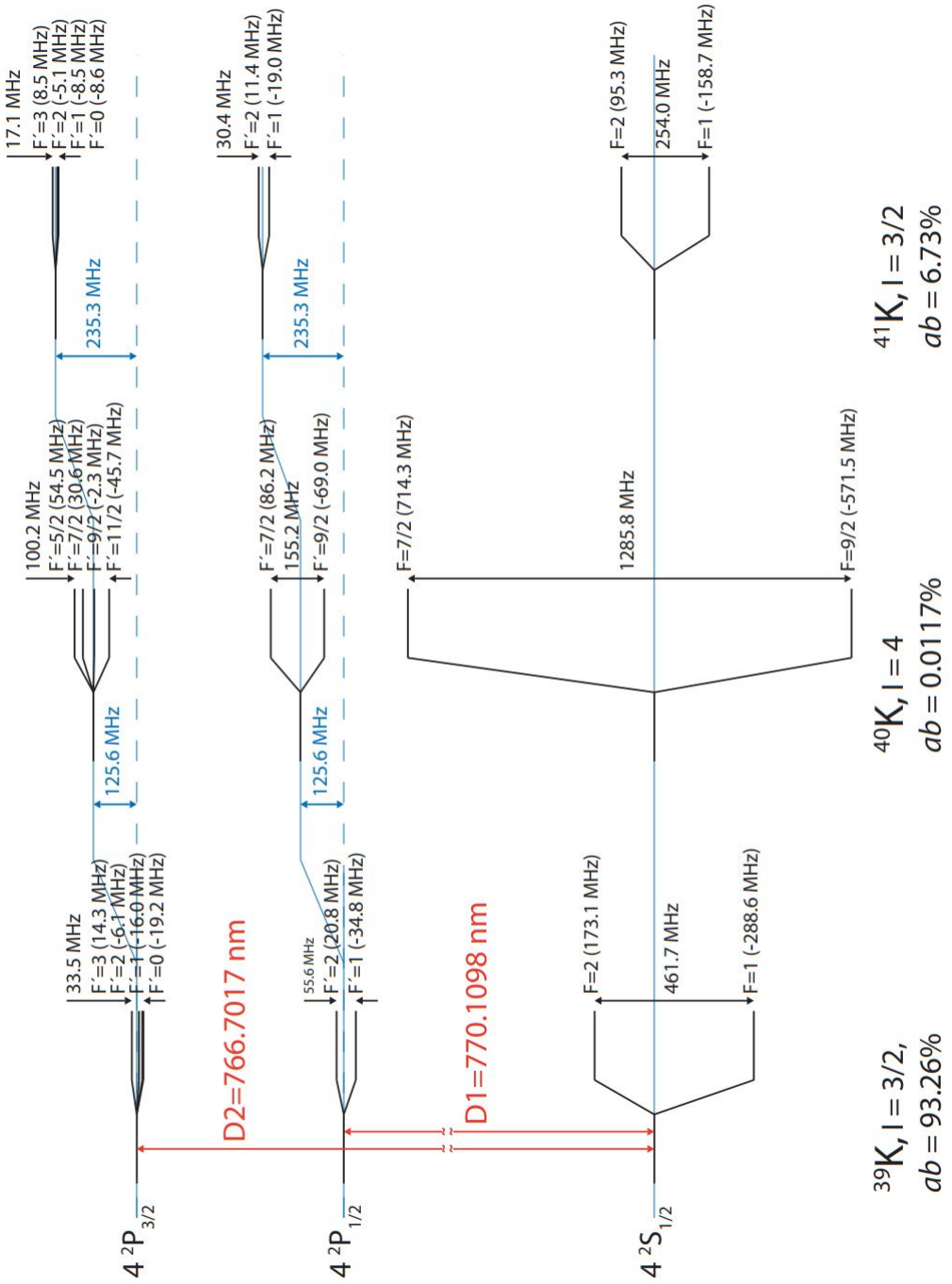

Figure 5.6: Energy levels of the D1 and D2-lines for ^{39}K, ^{40}K and ^{41}K. The abundance of the isotopes is given at the bottom. Adapted from [Wil09].

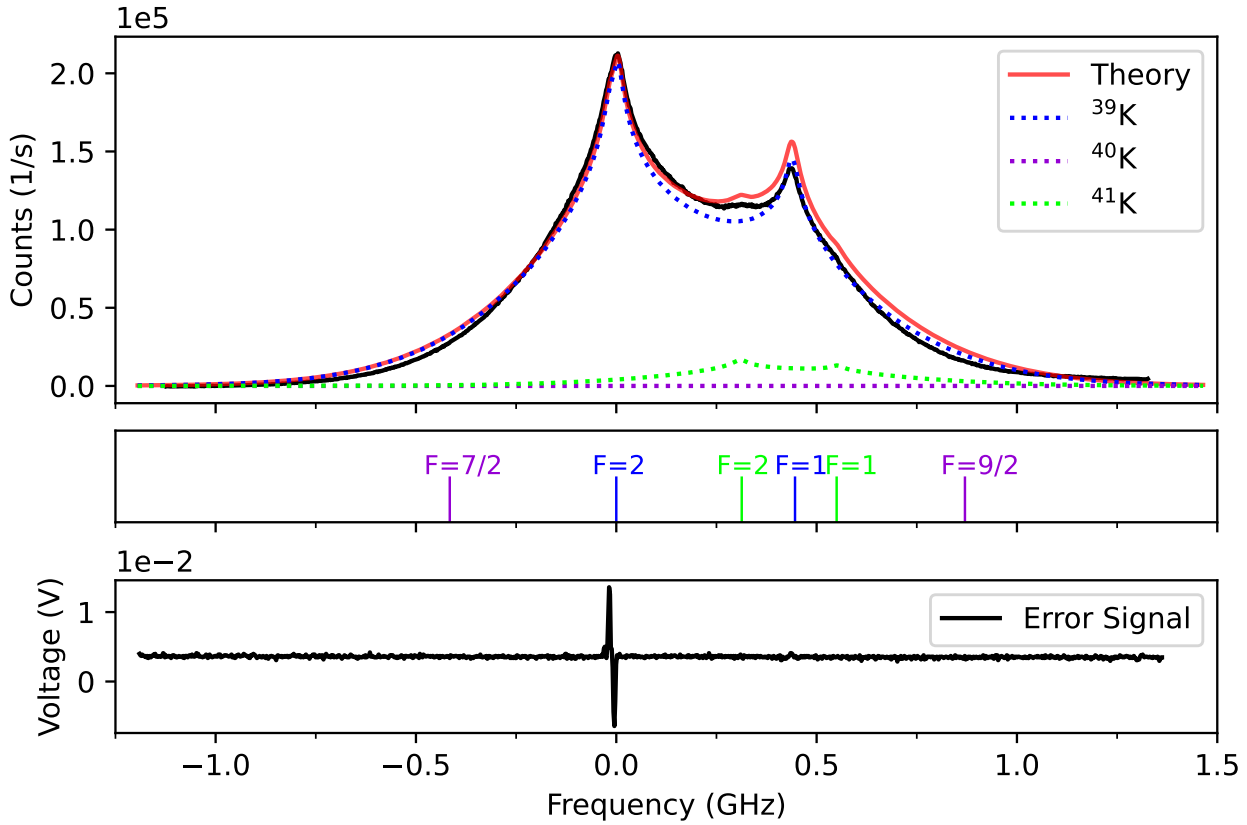

Figure 5.7: Transverse spectrum of potassium at $T = 114.5\,°\mathrm{C}$. In black the experimental data, in red our theoretical calculation. The colored dotted lines correspond to the contributions of the individual isotopes. In the mid panel the relevant transitions conntributing to the spectrum are shown and labeled with the angular momentum of their hyperfine groundstate. In the lowest panel the error signal used to calibrate the frequency axis is shown.

beam is always less than $0.063\,I_{\mathrm{sat}}$. For temperatures below $95\,°\mathrm{C}$ we operate the dispensers in a pulsed mode, as otherwise the reservoir gets hotter than the desired temperature[6]. Exploiting the mechanism deviated in section 5.1 we calculate the total flux for each spectrum. The result is shown in Fig. 5.8. Now the gray shaded area representing the uncertainty in temperature is narrower than in the graph for Li, as for lower temperatures the two thermocouples differ less from each other. The red line again corresponds to the theory. We can see that for the whole temperature range the gray shaded area is above the theory. Due to this consistent behaviour for all temperatures our assumption is, that inside the reservoir it might be hotter than the thermocouples located in the flanges indicate. This could well be due to the heating of the dispensers. We see that compared to lithium we hardly need power to heat the potassium reservoir with its coaxial heater, as the dispensers additionally heat from inside. As the thermocouples sit at least 1 cm away from the dispensers within the

[6]According to the datasheet on the website of the distributor, the dispensers reach a temperature of 600 K for a contact distance of 10 cm at an operating current of 3.7 A. In our reservoir this contact distance is less than 3 cm.

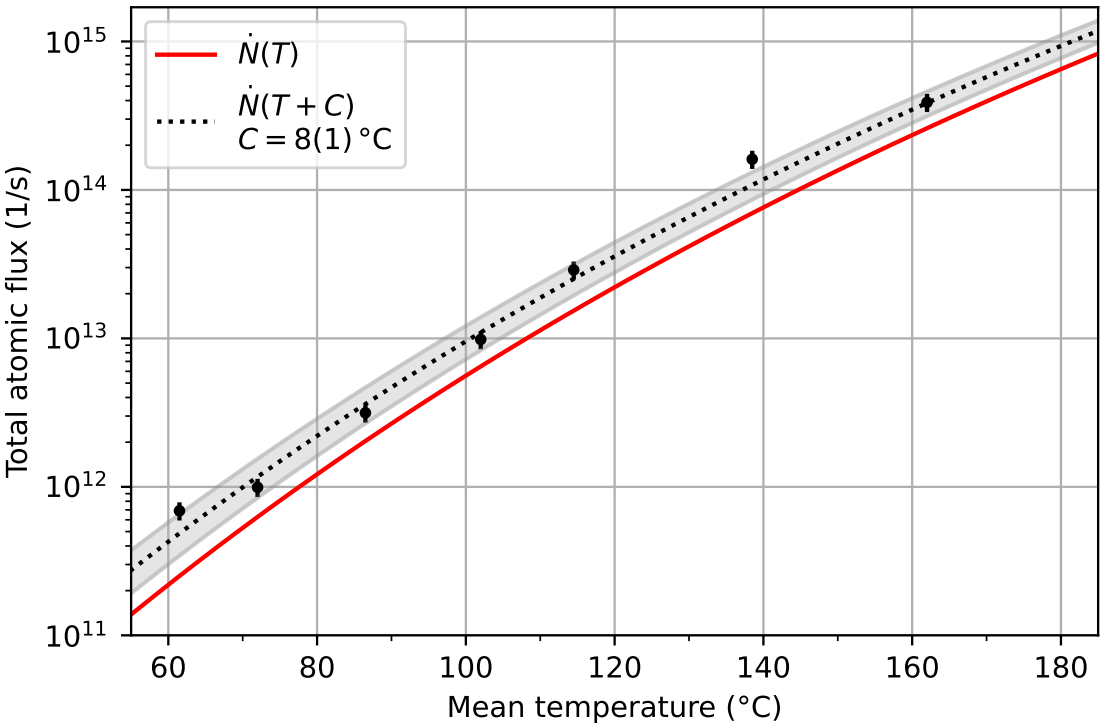

Figure 5.8: The total atomic flux of K emitted from the oven depending on the temperature in its reservoir. The red line is the theoretical expectation and the gray shaded area depicts the temperature uncertainty of our datapoints. The dotted black line is a fit to the data according to Eq. (2.12) where we add a free parameter C to the input temperature.

flanges, a temperature difference of a few degrees does not seem unlikely. To quantify this effect we fit our data with the same function the theory is calculated with but leave a free parameter C to shift the temperature $\dot{N} = \dot{N}(T + C)$. This fit is represented by the dotted black line. For our free parameter which indicates the temperature shift between our fitted data and the theory we get $C = 8(1)\,°C$. Again, the uncertainty of $\pm 2\,°C$ of the thermcouples has to be considered.

In the final assembly of the oven when it gets implemented into the main experiment we are going to have two dispensers containing 25 mg of K each. For $T_K = 90\,°C$ the flux according to the fit to our measurements is $4.7 \times 10^{12}\,s^{-1}$. Again assuming nonstop operation, this results in a lifetime of approximately 5.2 years. When we take into account that in the reservoir the actual temperature seems to be higher and hence operate the oven at eight degree less, the flux decreases and its lifetime increases to approximately 8.2 years.

6 Efficiency measurements

We now further investigate the shape of the atomic beam, more precisely its angular profile. Additionally, we measure the absolute intensity on the center-line. To do this, two major changes compared to the measurements shown in the previous chapter are introduced. First, we detect the atoms at a distance of $D = 62(1)\,\mathrm{cm}$ far away from the oven output. At this distance, the atomic beam has already expanded and we can spatially resolve its angular shape. Second, we install a narrow slit in the beam path of our setup that cuts the atomic beam into a thin sheet (see also Fig. 4.2). This allows us to measure its effective 1D profile. The evaluation of our data is then significantly simplified. Moreover, the data taken can be analyzed such that a quantitative conclusion about the efficiency of the source can be drawn.

6.1 Beam profile

We measure the beam shape in a distance of $D = 62(1)\,\mathrm{cm}$ to the oven nozzle. For a theoretical prediction we first calculate the intensity distribution in that x-y-plane. Therefore, we map every point in the plane described with coordiantes (ϑ, ϕ) onto cartesian coordinates (x, y), where $z = D$ is fixed. The coordinate transformation performs as follows.
We can write each of the coordinate pairs as

$$\vartheta = \arctan\left(\frac{R}{D}\right) \qquad x = R \times \cos(\phi) \tag{6.1}$$

$$\phi = \arcsin\left(\frac{y}{R}\right) \qquad y = R \times \sin(\phi) \tag{6.2}$$

where $R = \sqrt{x^2 + y^2}$ corresponds to the distance to the beam axis within the plane defined by $z = D$. Then the Jacobian determinant yields

$$J = \left|\frac{\partial(\vartheta, \phi)}{\partial(x, y)}\right| = \left|\begin{bmatrix} \frac{Dx}{R(D^2+R^2)} & \frac{Dy}{R(D^2+R^2)} \\ \frac{-y\,\mathrm{sgn}(x)}{R^2} & \frac{|x|}{R^2} \end{bmatrix}\right| = \frac{1}{R^2}\frac{D\left(x|x| + y^2\,\mathrm{sgn}(x)\right)}{R(D^2+R^2)}. \tag{6.3}$$

As the Jacobian is positive anyway, we can neglect the sign and modulus function, which simplifies it to

$$J = \frac{D}{R(D^2+R^2)}. \tag{6.4}$$

For every point in the x-y-plane we can thus calculate the corresponding intensity according to Eqs. (2.17) and (2.18), which is shown in the contour plot in the left panel of Fig. 6.1. The

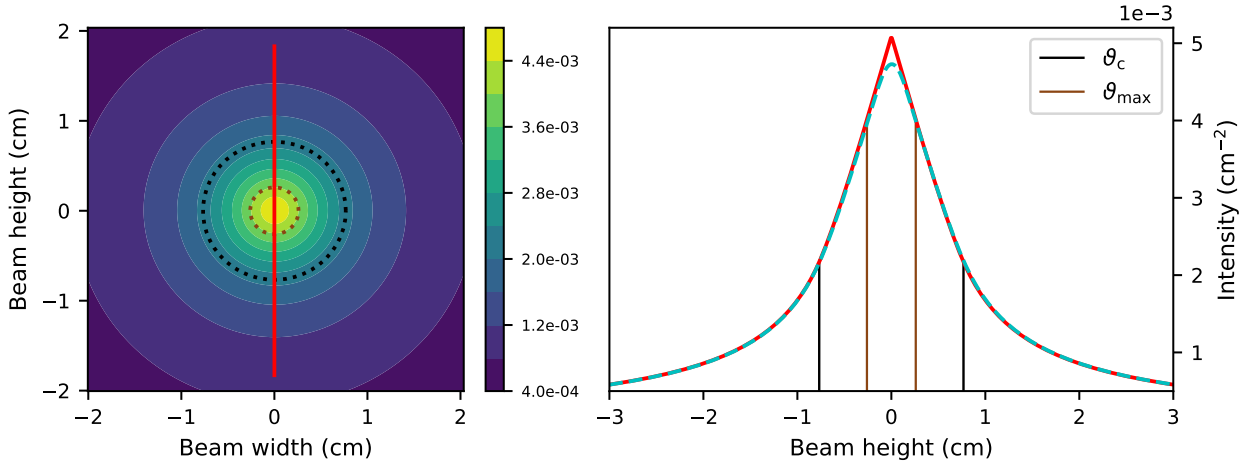

Figure 6.1: On the left, a contour plot illustrates the intensity of the atomic beam in the plane defined by $z = D$. The dotted black circle corresponds to the critical angle ϑ_c, the border betweeen type I and type II atoms. The dotted brown circle equals the maximum angle under which atoms can reach our MOT. On the right, a 1D cut through the contour plot along $x = 0$ is shown. The red line equals the data along the red line in the contour plot. The black and brown markers again correspond to ϑ_c and ϑ_{max}, respectively. For the dashed cyan line we convolute the contour plot with the cross sectional area of the potassium tube.

dimensions are in centimeters and the black circle corresponds to the critical angle ϑ_c. The brown circle shows the maximum angle under which atoms contribute to the MOT loading in the FeLiKx experiment ϑ_{max}. The right panel shows a cut through the contour plot along the red line at $x = 0$. Again, the black and brown lines mark ϑ_c and ϑ_{max}, respectively. The dashed cyan line takes into account that the atoms are not emitted from a point source but from a tube with diameter $a = 2.6\,\mathrm{mm}$. Herefore, we convolute the intensity distribution with the area of the tube.

6.2 Absolute intensity

Similar to the situation where we used the detected flourescence photons to infer the total flux emitted, we can also conclude on the center-line intensity I_0 and compare our data to theory. We use the same ansatz as in section 5.1.

$$\Phi_F = \sigma \iiint n(x, y, z) \times \Phi(y, z)\,\mathrm{d}x\,\mathrm{d}y\,\mathrm{d}z \tag{6.5}$$

and divide the atomic density by the area A such that, according to Eq. (5.1), it can be expressed by the intensity and their mean velocity $n(x, y, z) = \dot{N}/A\bar{v} = I/\bar{v}$. For the integration we can handle the axes individually. To facilitate the integration it is helpful to consider the sketch in Fig. 6.2. Here the situation we find ourselves in is schematically shown. Along the x-axis the integration is the simplest. The intensity of the laser beam is constant, if we assume absorption to be negligible. The intensity of the atomic beam we assume to

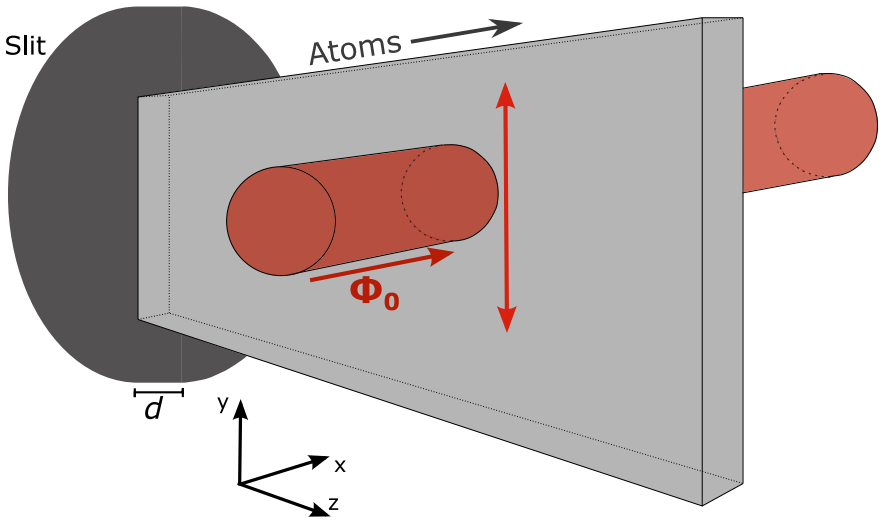

Figure 6.2: Schematic sketch of the interaction between atoms and laser light for the measurement of the atomic beam shape. The atomic beam is cut by the slit with width d and moves towards the viewer along the z-axis. The red laser light with photon flux Φ_0 has a Gaussian shape along the y/z-axis and intersects the atoms at 90° angle. A rotation stage enables us to move the laser beam vertically along the y-axis and scan the atomic distribution.

be constant too over the width of the slit, which amounts to 1.0(1) mm. Along the y-axis (vertical) the laser beam has a Gaussian shape with width w_L. The atomic beam intensity is distributed according to the beam profile plotted in the right panel of Fig. 6.1 with a width w_A. As $w_\mathrm{L} \ll w_\mathrm{A}$, we can assume the atomic beam intensity to be constant over that range. Along the z-axis the intensity of the atomic beam is approximately constant and the laser beam is again Gaussian. From these three considerations we see that the intensity of the atoms only depends on the x-coordinate and $I(z) = I_0 = I(y)$. The photon flux is Gaussian along the y/z-axis and $\Phi(x) = \Phi_0$. Plugging this into our ansatz yields

$$\Phi_\mathrm{F} = \frac{\sigma_0}{\bar{v}} \iiint I(x,y,z)\,\Phi(y,z)\,\mathrm{d}x\,\mathrm{d}y\,\mathrm{d}z \tag{6.6}$$

$$= \frac{\sigma_0}{\bar{v}} I_0 \underbrace{\int \Theta\left(\left|x - \frac{d}{2}\right|\right) \mathrm{d}x}_{=d} \underbrace{\iint \Phi(y,z)\,\mathrm{d}y\,\mathrm{d}z}_{=\Phi_0} = \frac{\sigma_0 I_0 d \Phi_0}{\bar{v}} \tag{6.7}$$

where d is the width of the atomic beam in x direction determined by the width of the slit and Θ is the Heaviside step function. This result is valid on resonance. If we scan the frequency such that the full peak is covered, we get an additional factor of $\Gamma/4(\delta\nu)$ and again we have to consider our factor ξ like in section 5.1, such that we end up at

$$\Phi_\mathrm{F} = \frac{\sigma_0 I_0 d \Phi_0}{\bar{v}} \xi \frac{\Gamma}{4(\delta\nu)} \iff I_0 = \frac{4\Phi_\mathrm{F}(\delta\nu)\bar{v}}{\xi\sigma_0\Gamma d\Phi_0}. \tag{6.8}$$

To compare this experimental result with theory we use Eqs. (2.3) and (2.4) in order to determine I_0. To account for the attenuation of the center-line that starts to happen as soon

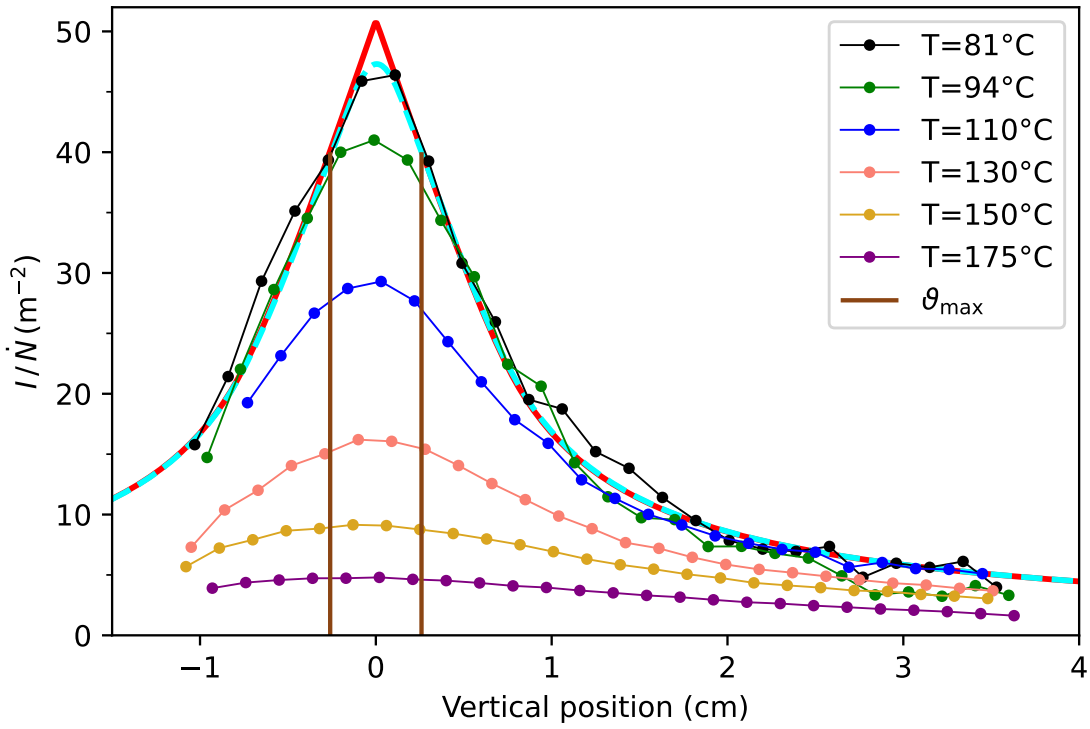

Figure 6.3: The shape of the potassium beam for different temperatures. The solid red and dashed cyan line are the ones from the right panel of Fig. 6.1 and correspond to the theory. The brown lines mark the maximum angle for the FeLiKx experiment $\vartheta_{\max}$. The curves are normalized to the flux at the respective temperature.

as we reach the opaque regime, we add the corresponding function according to Eq. (2.27), ending up at

$$I_0 = \frac{\dot{N}_{\cos}}{\pi D^2} \times A(n^*). \tag{6.9}$$

6.3 Potassium

In Fig. 6.3 we show our measurement data for the atomic beam shapes of potassium for different temperatures. On the y-axis we plot the absolute ratio from intensity to total flux. The red and cyan lines correspond to the theory from the right panel of Fig. 6.1. The black and green line correspond to temperatures in the transparent and on the edge to the opaque regime, respectively. For the other temperatures the oven is in the opaque regime with reduced densities between $n^* = 4.4$ for $T = 110\,^{\circ}\mathrm{C}$ and $n^* = 177$ for $T = 175\,^{\circ}\mathrm{C}$ according to Eq. (2.26). The black curve for $T = 81\,^{\circ}\mathrm{C}$ overlaps with our theory basically over the full distance. For positions below the peak (vertical position less than zero) and for positions between roughly 1 and 2 cm we see a slight deviation of too much signal. On the peak, the

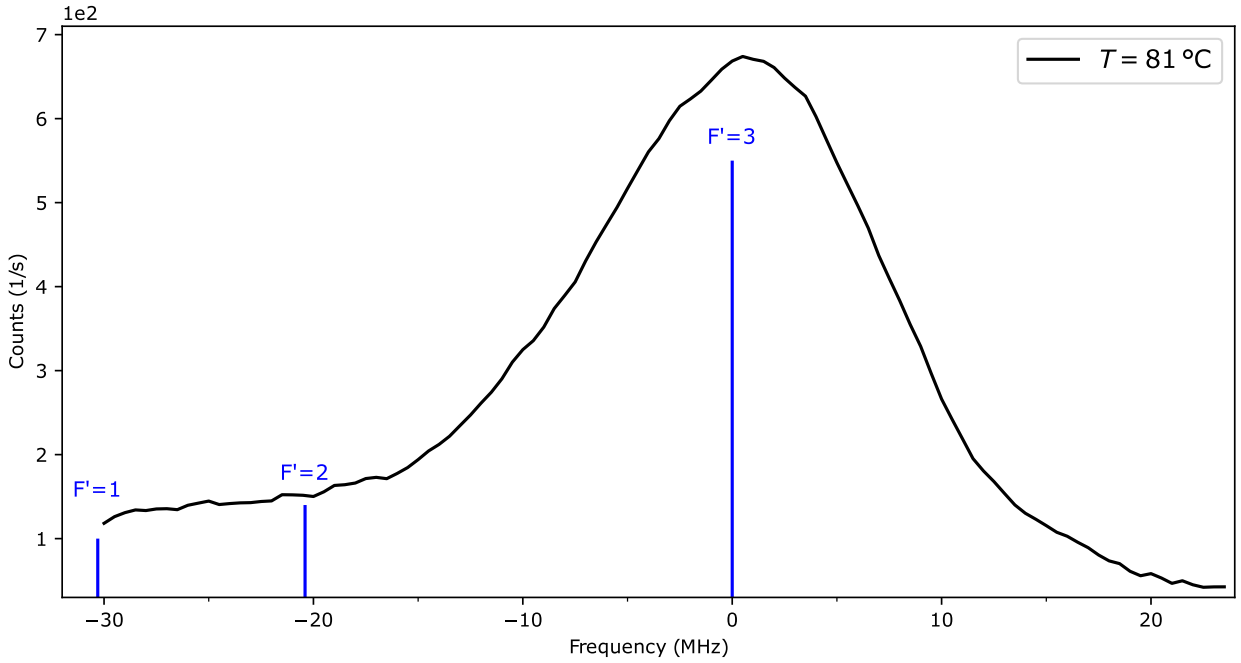

Figure 6.4: Frequency spectrum of the center-line of the potassium beam after the slit at $T = 81\,°\mathrm{C}$. The x-axis is shifted such that the peak is located at 0 MHz. The blue markers denote the excited hyperfine states of the three transitions contributing.

amplitude equals the one of our theory. For temperatures in the opaque regime the peak value decreases compared to the background. Type I atoms start to suffer from collisions and get scattered out of the beam axis resulting in a diminished center-line intensity just as shown in Fig. 2.5. The profile gets broader for higher temperatures until at $T = 175\,°\mathrm{C}$ only a large background is left. Here, hardly any atoms are able to pass through the tube collisionless anymore. The profiles in Fig. 6.3 show that a large fraction of the detected atoms emerge under an angle $\vartheta > \vartheta_{\max}$ and thus are not useful for us as they do not contribute to the MOT loading. In order to narrow the profile by pushing those atoms towards the center of the beam, a transverse cooling stage is going to be implemented after the oven nozzle.

From the measurements of the beam profile we know at which vertical position the peak of the atomic beam is located. In the next step we place the laser beam such that it hits the atomic peak and fix it at this position. Similar to the measurement of the flux in chapter 5 we perform a frequency scan but now by means of the DP-AOM from our optics setup. We scan around ±14 MHz in steps of 0.5 MHz (±28 MHz in steps of 1 MHz after the DP) around the resonance, such that we capture the whole transverse velocity distribution. We use the F=2 → F'=3 D2-line of K^{39} which is where the laser system is locked at. A sample spectrum for $T = 81\,°\mathrm{C}$ is shown in Fig. 6.4. The spectra for higher temperatures look similar with a larger amplitude. Compared to the same peak in Fig. 5.7 we can see that now its width is drastically reduced due to the slit in the beampath that blocks atoms with a transverse velocity. Nevertheless, it amounts to roughly three times the natural linewidth which can be

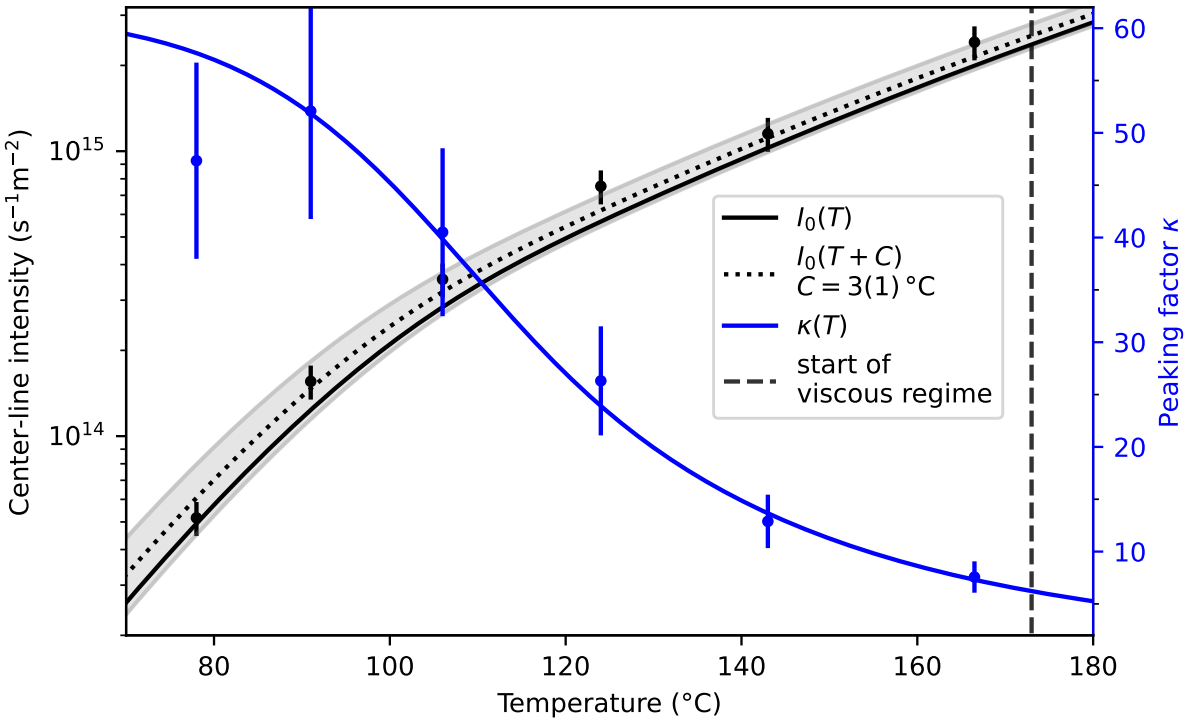

Figure 6.5: The center-line intensity I_0 (black) and the peaking factor κ (blue) of the potassium beam depending on the temperature in the reservoir. The theory line for the center-line intensity (black) is calculated according to Eq. (6.9) and the one for κ (blue) according to Eq. (2.15). The vertical dashed gray line marks the start of the viscous regime.

attributed to several factors. First, the slit is 1.0(1) mm wide and the atoms that pass still have a little transverse velocity component. Second, there are two more transitions from the F=2 ground state to F'=2 and F'=1 at lower frequencies whose signals contribute to our spectrum as denoted by the blue markers. Third, a slight asymmetry in the signal can occur due to an angle unequal to 90° between laser and atomic beam.

To calculate the center-line intensity via the mechanism derived in section 6.2, we integrate the frequency spectrum for each temperature. Our results are plotted as the black datapoints in Fig. 6.5 corresponding to the y-axis on the left. Again, the gray shaded area illustrates the temperature uncertainty of our data. The black theory curve is calculated using Eq. (6.9). Our datapoints of the center-line intensity are consistently above theory for the whole temperature range. This agrees with our measurement of the total emitted flux which is also above theory (see also Fig. 5.8). However, the temperature uncertainty of our datapoints fully overlaps with theory. To quantify the deviation of our datapoints from theory we follow the same procedure as in the flux measurements. We fit our data with the theoretical function supplemented with an offset C in the temperature as free parameter, which results in $C = 3(1)\,°\mathrm{C}$. This offset overlaps with the temperature uncertainty of the thermocouples of $\pm 2\,°\mathrm{C}$. Now the

offset is less than in Fig. 5.8 where we had an offset of 8(1) °C. One reason might be a slight systematic error in the vertical position of the laser beam. If it did not intersect the atomic beam at its peak, our center-line intensity would be lower. But more probable is that the atomic distribution within the reservoir was different in both measurements. In between, we disassembled the oven and refilled the reservoirs such that a temperature difference of a few degrees due to e.g. the exact angular position of the thermocouples relative to the dispensers is more than reasonable. We can clearly identify the start of the opaque regime at approximately 90 °C which is where the slope of our datapoints starts to decrease. The vertical dashed gray line marks the start of the viscous regime. From this point, the theoretical calculations are no longer valid.

Using these center-line intensity values we can now calculate the peaking factor κ according to Eq. (2.15). For the flux at the respective temperatures we take into account the offset from the fit. The results are shown as blue datapoints corresponding to the y-axis on the right. The blue solid line is the theory according to Eq. (2.15) with the theoretical values for $\dot{N}$ and I_0 plugged in. We see that our results are in accordance with theory except from the first datapoint at $T = 81\,°\mathrm{C}$. Its low magnitude is due to the fact that the flux at this temperature is particularly high (compare with Fig. 5.8). The large y-error bars are due to a relative error of about 20 %. When looking at our datapoints for κ, one sees most clearly the effect of increasing interatomic collisions due to a reduced mean free path in the opaque regime. The ratio of center-line intensity to total flux and such the efficiency decreases drastically. For the edge between transparent and opaque regime we can conclude that the efficiency of the potassium beam is indeed as expected.

7 Summary and Outlook

The goal of this thesis is to describe and test a new design of a dual species atomic source for lithium and potassium. In chapter 2 the theoretical foundation regarding atoms being emitted from a reservoir is introduced. We show how on the one hand the total flux of atoms is always linear in density and thus given by the temperature within the reservoir. On the other hand quantities characterizing the efficiency like the peaking factor start to decrease as soon the driving pressure reaches a value where the mean free path of the atoms equals the dimensions of the tube. Insights acquired from this theoretical point of view lead to the realization of a new design, which is supposed to fulfill the requirements from daily lab life.

Chapter 3 describes how our new oven is built. The principal idea for the design is set by location and size of the two reservoirs containing the atomic species. The species themselves specify the operating temperatures, that get monitored by seven K-type thermocouples distributed over the oven. We outline how the van der Waals coefficient determines the collisional cross-section of the species and such its mean free path. This intrinsic length scale determines the length for the tubes attached to the two reservoirs. We choose rather long tubes in order to avoid small radii, which did not prove useful in the past. The loading of the atoms happens in an improved way. Potassium is stored in two sealed dispensers, that simply get mounted into the reservoirs with screws. In contrast, the lithium comes as a wire in mineral oil. We clean it under argon atmosphere, scratch off its surface, wrap little pieces in steel meshes and fill them into the reservoir.

The experimental setup we use to test the functionality of the oven is described in chapter 4. First, the vacuum setup in terms of the detection volume, where atoms and light interact, is shown. Then we explain how the PMT is calibrated such that we are sure about the solid angle its sensitive area covers, which is important for absolute measurements. Last, we elaborate on the optical setup used for the different measurements and discuss the profile of the laser beam shaped by the Powell lens.

The measurements we did in order to determine the total flux being emitted from the oven are illustrated in chapter 5. For both species we find that the behaviour of the experimental data basically agrees with theory over the whole temperature range we probed. For lithium the measured flux is above theory for low temperatures and converges towards it with increasing temperature. The uncertainty range of our data overlaps with theory for all temperatures. For potassium the behaviour of the data is consistent for all temperatures but their magnitude is too high. For this reason we think that the temperature we measure with the thermocouples is roughly eight degrees too low, which seems reasonable as the potassium reservoir gets mainly heated by the dispensers located within. We conclude that at the temperatures we

Table 7.1: Comparison of the most important results of this thesis in terms of flux and efficiency of the atomic beams at the desired operating temperatures of $T_{\mathrm{K}} = 90\,^{\circ}\mathrm{C}$ and $T_{\mathrm{Li}} = 350\,^{\circ}\mathrm{C}$ with their theoretical expectations.

	Theory	Experimental
$\dot{N}(\mathrm{K})$	$2.67 \times 10^{12}\,\mathrm{s}^{-1}$	$4.7(7) \times 10^{12}\,\mathrm{s}^{-1}$
$\kappa(\mathrm{K})$	52	52(10)
Lifetime K	9 y	> 5.2 y
$\dot{N}(\mathrm{Li})$	$1.2 \times 10^{13}\,\mathrm{s}^{-1}$	$1.9(2) \times 10^{13}\,\mathrm{s}^{-1}$
Lifetime Li	35 y	> 21.5 y

plan for continuous operation, the oven is going to run for at least five years without reloading, limited by the amount of potassium that is stored within the dispensers.

In chapter 6 we show the measurements regarding the efficiency of the potassium beam emitted from our oven. Considering the data for the atomic beam shape at different temperatures we can clearly see the attenuation of the center-line intensity for temperatures in the opaque regime. The peak we observe for lower temperatures gets more and more lost the higher the temperature until only a broad background is left. For temperatures in the transparent regime the amplitude of the beam shape agrees with theory. From the absolute determination of the center-line intensity, which is consistently above theory just as the flux before, we calculate the peaking factor. Except for the datapoint with the lowest temperature which is too low, our data for κ agrees with theory. Table 7.1 breaks our experimental results down into the most important numbers useful for further operation of the oven and compares their magnitude to theory.

The next step is the measurement of the beam shape and the center-line intensity also for lithium. As there is no experimental value of the van der Waals coefficient for lithium yet, our aim is to experimentally determine its magnitude. After that we implement and test a transverse cooling stage in front of the oven nozzle, which is predicted to enhance the center-line intensity by a factor of 40 according to our calculations. Additionally, we install a flux-meter in the beam path after the transverse cooling for a continuous surveillance of the emitted flux during operation. Eventually, the oven with its transverse cooling stage and flux-meter is going to be implemented into the main experiment and we are going to change to isotopically enriched potassium and lithium.

Bibliography

[Alc84] C. B. Alcock et al. "Vapour Pressure Equations for the Metallic Elements: 298-2500K". *Can. Metall. Quart.* **23** (1984), pp. 309–313.

[And95] M. H. Anderson et al. "Observation of Bose-Einstein condensation in dilute atomic vapor". *Science* **269** (1995), pp. 198–201.

[Bei75] H. C. W. Beijerinck and N. F. Verster. "Velocity distribution and angular distribution of molecular beams from multichannel arrays". *J. Appl. Phys.* **46** (1975), pp. 2083–2091.

[Bow16] W. Bowden et al. "An adaptable dual species effusive source and Zeeman slower design demonstrated with Rb and Li". *Rev. Sci. Instrum.* **87** (2016), p. 043111.

[Buc65] U. Buck and H. Pauly. "Messungen des van der Waals-Potentials zwischen Alkaliatomen". *Zeitschrift für Physik* **185** (1965), pp. 155–168.

[Chu86] S. Chu et al. "Experimental Observation of Optically Trapped Atoms". *Phys Rev Lett* **57** (1986), pp. 314–317.

[Cla30a] P. Clausing. "Über das Kosinusgesetz der Zurückwerfung als Folge des zweiten Hauptsatzes der Thermodynamik". *Ann. Phys. (Berl.)* **396** (1930), pp. 533–566.

[Cla30b] P. Clausing. "Über die Strahlformung bei der Molekularströmung". *Z. Angew. Phys.* **66** (1930), pp. 471–476.

[Cla32] P. Clausing. "Über die Strömung sehr verdünnter Gase durch Röhren von beliebiger Länge". *Ann. Phys. (Berl.)* **404** (1932), pp. 961–989.

[Cro69] D. J. Croucher and J. L. Clark. "Total collision cross sections and van der Waals constants for alkali atom interactions with atoms and non-reactive diatomic molecules at thermal energies". *J. Phys. B: At. Mol. Phys.* **2** (1969), pp. 603–623.

[Dav20] E. T. Davletov et al. "Machine learning for achieving Bose-Einstein condensation of thulium atoms". *Phys Rev A* **102** (2020), p. 011302.

[Fon61] P. R. Fontana. "Theory of Long-Range Interatomic Forces. I. Dispersion Energies between Unexcited Atoms". *Phys. Rev.* **123** (1961), pp. 1865–1870.

[Fri12] A. Frisch et al. "Narrow-line magneto-optical trap for erbium". *Phys. Rev. A* **85** (2012), p. 051401.

[Fri21] I. Fritsche et al. "Stability and breakdown of Fermi polarons in a strongly interacting Fermi-Bose mixture". *Phys. Rev. A* **103** (2021), p. 053314.

[Geh03] M. E. Gehm. "Preparation of an optically-trapped degenerate Fermi gas of ^{6}Li: Finding the route to degeneracy". PhD thesis. Duke University, 2003.

[Gio60] J. A. Giordmaine and T. C. Wang. "Molecular Beam Formation by Long Parallel Tubes". *J. Appl. Phys.* **31** (1960), pp. 463–471.

[Ham21] Hamamatsu. *Final Test Sheet - Photomultiplier Tube*. Hamamatsu Photonics. 2021.

[Han60] G. R. Hanes. "Multiple Tube Collimator for Gas Beams". *J. Appl. Phys.* **31** (1960), pp. 2171–2175.

[Heo12] M.-S. Heo et al. "Formation of ultracold fermionic NaLi Feshbach molecules". *Phys. Rev. A* **86** (2012), p. 021602.

[Kem16] S. L. Kemp et al. "Production and characterization of a dual species magneto-optical trap of cesium and ytterbium". *Rev. Sci. Instrum.* **87** (2016), p. 023105.

[Koh12] C. Kohstall et al. "Metastability and coherence of repulsive polarons in a strongly interacting Fermi mixture". *Nature (London)* **485** (2012), pp. 615–618.

[Kur81] M. V. Kurepa and C. B. Lucas. "The density gradient of molecules flowing along a tube". *J. Appl. Phys.* **52** (1981), pp. 664–669.

[Lew31] L. C. Lewis. "Die Bestimmung des Gleichgewichts zwischen den Atomen und den Molekülen eines Alkalidampfes mit einer Molekularstrahlmethode". *Zeitschrift für Physik* **69** (1931), pp. 786–809.

[Mas34] H. S. W. Massey and C. B. O. Mohr. "Free paths and transport phenomena in gases and the quantum theory of collisions. II.—The determination of the laws of force between atoms and molecules". *Proc. R. Soc. London A.* **144** (1934), pp. 188–205.

[Met99] H. J. Metcalf and P. van der Straten. *Laser Cooling and Trapping*. Springer, New York, 1999.

[Mil88] P. W. Milonni and J. H. Eberly. *Lasers*. Wiley, 1988.

[Miy22] Y. Miyazawa et al. "Bose-Einstein Condensation of Europium". *ArXiv e-prints* (2022), p. 2207.11692v2.

[Mod02] G. Modugno et al. "Collapse of a degenerate Fermi gas". *Science* **297** (2002), pp. 2240–2243.

[Ner20] E. Neri et al. "Realization of a cold mixture of fermionic chromium and lithium atoms". *Phys. Rev. A* **101** (2020), p. 063602.

[Ola70] D. R. Olander and V. Kruger. "Molecular Beam Sources Fabricated from Multichannel Arrays. III. The Exit Density Problem". *J. Appl. Phys.* **41** (1970), pp. 2769–2776.

[Raa87] E. L. Raab et al. "Trapping of Neutral Sodium Atoms with Radiation Pressure". *Phys. Rev. Lett.* **59** (1987), pp. 2631–2634.

[Ram85] N. F. Ramsey. *Molecular Beams*. Oxford Univ. Press, 1985.

[Rav18] C. Ravensbergen et al. "Production of a degenerate Fermi-Fermi mixture of dysprosium and potassium atoms". *Phys. Rev. A* **98** (2018), p. 063624.

[San11] C. J. Sansonetti et al. "Absolute Transition Frequencies and Quantum Interference in a Frequency Comb Based Measurement of the ^{6,7}Li D Lines". *Phys. Rev. Lett.* **107** (2011).

[Sch12] M. Schioppo et al. "A compact and efficient strontium oven for laser-cooling experiments". *Rev. Sci. Instrum.* **83** (2012), p. 103101.

[Sen15] R. Senaratne et al. "Effusive atomic oven nozzle design using an aligned microcapillary array". *Rev. Sci. Instrum.* **86** (2015), p. 023105.

[Spi10] F. M. Spiegelhalder et al. "All-optical production of a degenerate mixture of ^{6}Li and ^{40}K and creation of heteronuclear molecules". *Phys. Rev. A* **81** (2010), p. 043637.

[Sta05] C. A. Stan and W. Ketterle. "Multiple species atom source for laser-cooling experiments". *Rev. Sci. Instrum.* **76** (2005), p. 063113.

[Tie09] T. G. Tiecke. "Feshbach resonances in ultracold mixtures of the fermionic quantum gases ^{6}Li and ^{40}K". PhD thesis. University of Amsterdam, 2009.

[Tra18] A. Trautmann et al. "Dipolar Quantum Mixtures of Erbium and Dysprosium Atoms". *Phys. Rev. Lett.* **121** (2018), p. 213601.

[Wal03] J. Walls et al. "Measurement of isotope shifts, fine and hyperfine structure splittings of the lithium D lines". *Eur. Phys. J. D* **22** (2003), pp. 159–162.

[Wil09] E. Wille. "Preparation of an Optically Trapped Fermi-Fermi Mixture of ^{6}Li and ^{40}K Atoms and Characterization of the Interspecies Interactions by Feshbach Spectroscopy". PhD thesis. Innsbruck University, 2009.